ABSTRACT

Title of dissertation: DIAMAGNETISM OF A SUPERSONIC ROTATING MAGNETIZED PLASMA

William Young, Doctor of Philosophy, 2012

Dissertation directed by: Professor Adil Hassam
Department of Physics

The Maryland Centrifugal Experiment (MCX) combines supersonic rotation with a magnetic mirror geometry to centrifugally confine a hydrogen plasma with the goal of investigating a magnetic confinement scheme applicable as a fusion reactor.

To demonstrate this axial confinement of plasma by centrifugal forces, an axial array of magnetic loops was installed, external to the vacuum vessel, to measure the axial and radial components of the magnetic field expelled by the plasma. The diamagnetic measurements show concentration of plasma pressure at locations of magnetic minima, as expected for centrifugal confinement.

Additionally, a visible light, multichord spectrometer was upgraded to ten chords allowing for the measurement of plasma rotation and temperature profiles with increased precision. Improved deconvolution techniques are investigated to further increase the precision of radial profiles calculated from multichord measurements.

A perturbative, ideal MHD equilibrium solution is then developed to relate the diamagnetic measurements to density, rotation, and temperature profiles of the plasma. This solution, along with density measurements by interferometery, is used to estimate rotation velocity and temperature of the plasma from magnetic data, and then is compared to spectroscopic measurements of rotation velocity and temperature radial profiles. Agreement

between spectroscopic measurements and magnetic measurements via the MHD solution further demonstrate the presence of centrifugal confinement and its efficacy.

DIAMAGNETISM OF A SUPERSONIC ROTATING MAGNETIZED PLASMA

by

William Young

Dissertation submitted to the Faculty of the Graduate School of the
University of Maryland, College Park in partial fulfillment
of the requirements for the degree of
Doctor of Philosophy
2012

Advisory Committee:
Professor Adil Hassam, Chair/Advisor
Professor Richard Ellis
Professor Christopher Davis
Dr. John Rodgers
Professor William Dorland

Dedication

To my wife for her unending support and to my family who set me off on the path to where I am now.

Acknowledgments

I am thankful for the insight and patience shared by my advisor Adil Hassam and by Rick Ellis. I would like to thank Catalin Teodorescu and Ryan Clary, for teaching me the day-to-day aspects of MCX. I am also thankful of Carlos Romero-Talamas and Remington Reid, for their discussions and help with MCX operations, Ilker Uzun-Kaymak and Sarah Messer, for keeping work around MCX interesting. I would especially like to thank Ray Elton, John Rodgers, and Jay Pyle, for their help in all things spectroscopic, electrical, and mechanical, respectively.

Table of Contents

List of Tables

List of Figures

List of Associated Publications

W. C. Young, S. Choi, M. R. Clary, R. F. Ellis, A. B. Hassam, C. Teodorescu, and I. Uzun-Kaymak. The Diamagnetism of Rotating Plasmas. Poster presented at: APS - 50th Annual Meeting of the Division of Plasma Physics; 2008 Nov 17-21; Dallas, TX.

W. C. Young, M. R. Clary, R. F. Ellis, A. B. Hassam, G. Swan, C. A. Romero-Talamás, C. Teodorescu, and I. Uzun-Kaymak. The Diamagnetism of Rotating Plasmas in a Shaped Magnetic Field. Poster presented at: APS - 51st Annual Meeting of the Division of Plasma Physics; 2009 Nov 2-6; Atlanta, GA.

W. C. Young, M. R. Clary, R. F. Ellis, A. B. Hassam, G. Swan, R. Reid, C. A. Romero-Talamás, C. Teodorescu, and I. Uzun-Kaymak. The Diamagnetism of Rotating Plasmas in Shaped Magnetic Fields. Invited talk at: Innovative Confinement Concepts Workshop; 2010 Feb 16-19; Princeton, NJ.

C. Teodorescu, W. C. Young, G. W. S. Swan, R. F. Ellis, A. B. Hassam, and C. A. Romero-Talamás. Confinement of plasma along shaped open magnetic fields from the centrifugal force of supersonic plasma rotation. *Phys. Rev. Lett.*, 105(8):085003, Aug 2010.

W. C. Young, M. R. Clary, R. F. Ellis, A. B. Hassam, R. Reid, G. Swan, C. A. Romero-Talamás, G. Taylor, C. Teodorescu, and I. Uzun-Kaymak. MHD Equilibrium and Diamagnetism of Rotating Plasmas in Shaped Magnetic Fields. APS - 52nd Annual Meeting of the Division of Plasma Physics; 2010 Nov 8-10; Chicago, IL.

W. C. Young, A. B. Hassam, C. A. Romero-Talamas, R. F. Ellis, and C. Teodorescu. Diamagnetism of rotating plasma. *Phys. Plasmas* 18:112505, 2011.

W. C. Young, C. A. Romero-Talamás, R. Reid, R. F. Ellis, and A. B. Hassam. Magnetic Structure of the Maryland Centrifugal Experiment. APS - 53rd Annual Meeting of the Division of Plasma Physics; 2011 Nov 14-18; Salt Lake City, UT.

C. A. Romero-Talamás, R. C. Elton, W. C. Young, R. Reid, and R. F. Ellis. Isorotation and differential rotation in a magnetic mirror with imposed ExB rotation. *Phys. Plasmas*, Accepted for publication May 29th, 2012.

Chapter 1

Introduction

1.1 Background

The fundamental motivation of the Maryland Centrifugal Experiment (MCX) [1] is to investigate a novel magnetic confinement scheme for fusion plasmas. If the complexities and costs of production of a fusion reactor could be reduced, the plentiful fuel and low waste production would make fusion a near ideal source of energy.

While most magnetic confinement geometries employ closed magnetic fields that spatially localize the Larmor orbits of charged particles, open field line configurations require simpler magnetic coil construction at the expense of having to deal with locations where field lines intersect with walls of the vessel. An example of an open magnetic confinement scheme is the magnetic mirror, using an axial magnetic field with a minimum located between two maxima. This confines particles due to the adiabatic invariance of the magnetic moment, $\mu = mv_{\perp}^2/2B$, where $v_{\perp}$ is the velocity perpendicular to the magnetic field. Particles with a large enough velocity parallel to the magnetic field, $v_{||}$, are still lost through a loss cone in phase space where $v_{||}/v_{\perp} > \sqrt{R_m - 1}$. Here $R_m = B_{max}/B_{min}$ is the mirror ratio, the ratio of the sstrongest magnetic field to the weakest field along the central axis. Eventually in a collisional systen, even particles outside the loss cone are loss due to collisions repopulating the loss cone with previously trapped particles.

If a radial electric field is added to the axial magnetic field of a magnetic mirror, the crossed fields will drive a rotation via $\mathbf{E} \times \mathbf{B}$ drift. In the rotating frame, the particles will experience an outward centrifugal force, which due to the bowed nature of the

magnetic field lines, includes a component along the magnetic field lines toward the center of the machine. This provides a centrifugal confinement that can maintain a pressure gradient along the field lines and close the loss cone. [2, 3] While the outward force could lead to interchange instability, a high enough velocity shear that results from drag by the boundaries of the plasma would stabilize against this instability [4, 5]. The MCX machine consists of such a configuration, with a radial electric field generated by an axial, conducting core down the center of a mirror machine that is biased relative to a cylindrical vacuum vessel.

1.2 Motivation

This thesis will address two aspects of work on MCX: operation and results of a variety of diagnostics investigating plasma diamagnetism in rotating mirrors, and how MHD theory ties those results together.

Central to any experimental plasma physics experiment is its array of diagnostics that provide access to the variety of plasma parameters. One of the primary goals of MCX is to demonstrate axial confinement of plasma, and a straightforward way to demonstrate this is to measure density at the axial center (midplane) and away from the center. A pair of interferometers measure density at these locations, producing both an absolute measurement of densities involved, and relative, rough measurement of axial density gradient [6]. Another important aspect of MCX is the rotation velocity, as the sonic Mach number will be shown to be a critical parameter in centrifugal confinement. Via Doppler shift of atomic spectral lines, spectroscopy over multiple chords measure both rotation velocity and radial profile of the rotation velocity. The profile has the additional benefit of demonstrating the presence of velocity shear, which has been shown as necessary for stabilization

of interchange instabilities [7]. The final set of diagnostics to be discussed are magnetic loops that measure the field lines expelled by plasma pressure. Large loops external to the vacuum vessel can measure slow time scale changes in flux suitable for examining plasma equilibrium. An array of these loops results in an axial profile of the diamagnetism and hence the plasma pressure, additionally demonstrating axial confinement of plasma with more granularity than a pair of interferometers.

Individually, the results of these diagnostics provide insight into important aspects of MCX, but also can be utilized together to test the validity of a perturbative MHD theory to MCX. MHD equations in cylindrical coordinates, with some basic assumptions, results in a variation of the Grad-Shafranov equation [8] that includes additional diamagnetism from supersonic rotation. This equation relates the profiles of rotational velocity, temperature, and density to an expected diamagnetism, similar to such reconstructions used on tokamaks. This form of the Grad-Shafranov equation is similar to those seen in other axisymmetric confinement schemes with rotation [9,10] and even analysis of astrophysical plasmas such as the Jovian magnetosphere [11,12] or accretion discs [13].

1.3 Structure of Thesis

The second chapter of this thesis will cover the general experimental setup of the MCX machine and required systems. This includes a discussion of calibrating and measuring the structure of the vacuum magnetic field as needed later for calibrating diamagnetic measurements and for the MHD modeling. In particular, Section 2.3.5 explains the significance of using mirror ratios 7.8 and 3.2. Additionally, there is a brief discussion of upgrades to the MCX capacitor bank.

The three following chapters will introduce the three diagnostic methods discussed:

interferometery, spectroscopy, and diamagnetic loops. These chapters cover background, operation, and basic results from those diagnostics. Chapter 6 then derives a perturbative solution to MHD for MCX and develops a numeric method to find the solution. Following in Chapter 7 is analysis and interpretation of the diagnostic results in context of the MHD solution.

Finally, there is a chapter covering a brief discussion of measurements of B_θ, the magnetic field in the azimuthal direction.

Chapter 2

Experiment Setup

2.1 General Setup

Figure 2.1 shows a simplified cross-section of the physical setup of the MCX experiment. The geometry of the vacuum vessel is discussed in section 2.2 and the magnets discussed in the following section 2.3. The right of the diagram shows a simplified electrical schematic of the capacitor bank used both for breakdown and driving rotation (see figure 2.2 for an example plasma voltage and current). The capacitor bank and electrical components, including the data acquisition system, are discussed in the last two sections of this chapter.

2.2 Vacuum Vessel and Core

The design of the vacuum vessel and core influence quite a few aspects of the experiment as they limit the location of diagnostics and limit the extent of the plasma. The vacuum vessel is composed of 304 stainless steel, which has a resistivity of $7.2 \times 10^{-5}\Omega$·cm and a relative magnetic permeability of 1.005-1.02 [14].

The vessel is cylindrical, but has three different radii for different z locations. Within 65 cm of the midplane, there is an inside radius of 27.6 cm, while further from the midplane this reduces to 22.5 cm, then finally 18.7 cm (corresponding to outer diameters of 22, 18, and 15 inches, with 1/8 inch thick vessel walls). As no other radial plasma limiting structure is used, the outermost extent of the plasma is determined by which magnetic field lines intersect the vacuum vessel (referred to as Last Good Flux Surface, LGFS),where

the conducting vacuum vessel shorts out the electric field driving rotation for outer field lines. For mirror ratios below about 8.8, the LGFS contacts the vacuum vessel at the corner at the z=65 cm change in radius. Higher mirror ratios will contact the vessel at the midplane. The exact boundary may be lower due to outward bowing of field lines from the plasma. Similarly, the innermost LGFS is determined by the field lines that intersect with the core, which has a uniform diameter of 5.1 cm.

In between the inner and outer LGFS, the field lines intersect alumina insulators within the mirror throats. These consist of several concentric cylinders, such that the radial cross-section looks like a comb, in order to maximize the path length of any conduction along the surface of the insulator, minimizing any surface conduction there. [15]

The locations of many diagnostics are limited to where there are vacuum ports within the vessel. There are three rings of ports with unobstructed visibility/access to the plasma: one set at the midplane, and then one toward each end at $z = \pm 85$ cm. These are the three z locations internal probes can be placed without large installation efforts, and similarly the location for external observations like spectroscopy or interferometry (the latter additionally being limited in r to avoid signal being blocked by the core).

2.3 Magnets

2.3.1 Physical Setup

There are two pairs of magnets, each with independent power supplies. The stronger set, often referred to as the "O-coils," located at z=110-150 cm provide the main mirror field of up to 15.5 kG at the mirror throat (center of one of the outer magnets). These outer magnets are powered by an Eratron brand, unfiltered three-phase SCR DC power supply, depending on the magnet inductance to remove fluctuations. While the bulk magnetic

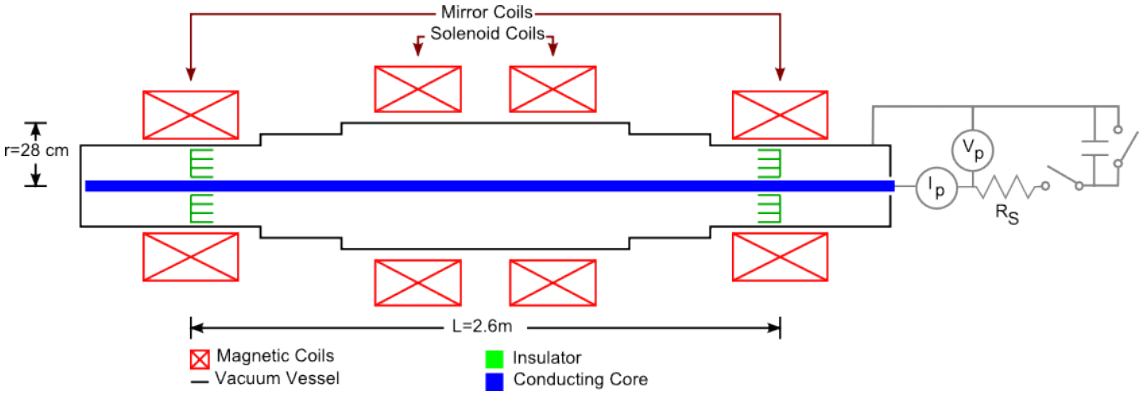

Figure 2.1: A simple overview of the MCX configuration. The mechanical portion is axisymmetric along a centerline through the core (in blue). The middle section has the largest inner radius at 27.6 cm, followed by 22.5 cm and 18.7 cm for the other sections. A simplified circuit on the right shows the capacitor bank, with the voltage and current measurements, a series resistance R_S typically of 2Ω, and the switches for connecting the bank to start the discharge and to short out and stop the discharge.

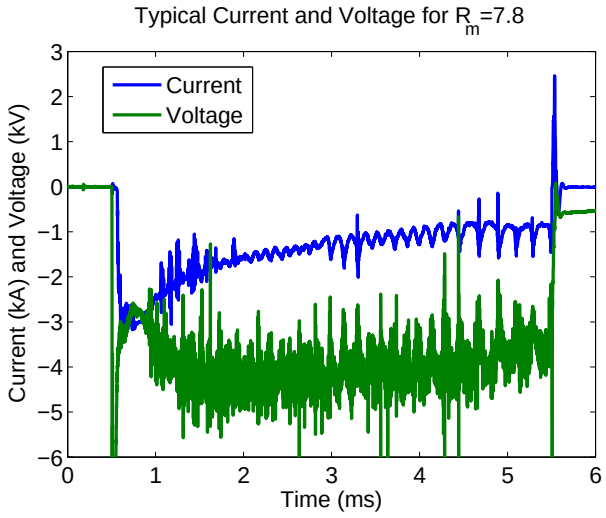

Figure 2.2: Here is a typical mirror ratio 7.8 plasma voltage and current, with a voltage of about 3.9 kV and current of about 1.0 kA toward the end of the shot.

field created by these magnets is stabilized and DC by the time the plasma is created, there is a 360 Hz, non-sinusoidal noise emitted in the close vicinity, discussed in a later section. The current of these outer magnets is not set directly, but instead the power supply is fed a control voltage from 0-4 V that must be calibrated for the corresponding current.

The second set of coils, named MS-coils, are located at z=20-40 cm, and provide a smaller solenoid field of up to 2.5 kG, used to adjust the mirror ratio of the setup from ratio 22 (the second set completely off) down to ratios as low as 2 or 1. The two coil sets are controlled independently which allows for selection of both a mirror ratio and strength at the center of midplane. The most common nominal magnetic settings for shots are a midplane strength, B_{mid}, of 2 kG, and the mirror ratio, $R_m = B_z(r = 0, z = 130cm)/B_z(r = 0, z = 0)$, at 7 (see following calibration section for why these are nominal and not actual settings). Occasionally mirror ratio is changed while maintaining the same midplane field, to ratios such as 3 and 5, while less frequently other values of mirror ratio or midplane field are used. Lower mirror ratios are avoided due to the higher current required and risk of damage to the MS-coils. In at least one case, higher fields caused arcing within these coils, suspected to be due to higher fields causing the component coils to shift and contact the metal casing. Very high mirror ratios and low midplane fields are also avoided, as requiring a very low current from the power supply for the MS-coils can sometimes allow current reversal/bouncing during turn-on due to mutual inductance between the two sets of coils.

During a typical shot process the MS coil supply is turned on first, with the O-coil supply turned on 5 seconds later. The MS coil supply ramps up with an L/R time of about 1.08 seconds (after a 4 second delay from the power supply), while the O-coil has a linear

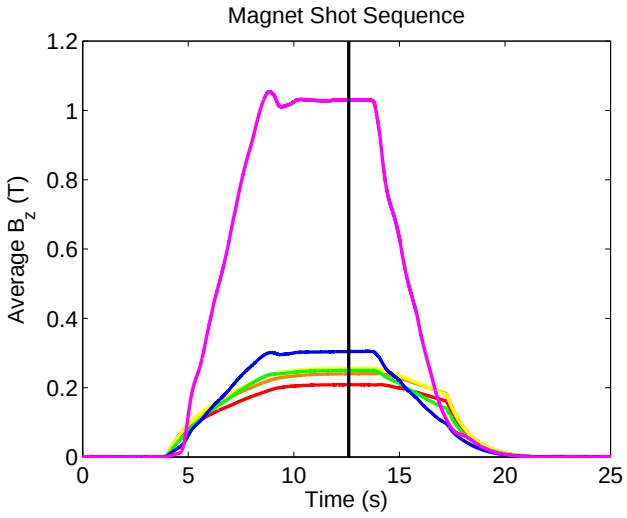

Figure 2.3: An example of the magnet ramp up and shut down speeds for mirror ratio 7. Curves are colored from red for innermost, $z = 8$ cm, to purple for the outermost at $z = 102$ cm. The vertical black line shows the time plasma discharge takes place.

ramp-up over about 4 seconds, with some bouncing after peak value is reached. A plasma shot is taken about 4 seconds after the peak O-coil current is reached (about 5 bounce oscillation time periods) when the currents have leveled (see figure 2.3). The O-coil is then switched off first, followed by the MS coil. Both are not switched on at the same time to prevent inductive coupling from confusing the regulation of either, and the on time for the O-coil power is minimized due to the power dissipated by the coils. While the O-coil power supply typically operates in constant current mode, the MS power supply operates in a constant voltage mode due to large oscillations that developed otherwise from the mutual inductance of the systems.

The fields created by these magnets are calculated by a simple code treating each magnet as set of circular loops in an evenly spaced array within measured volumes of the

coils. The field from each coil is calculated in terms of the vector potential [16]:

$$rA_\phi = \frac{\mu_0 I}{2\pi}\sqrt{ar}M[(2-M)K(M) - 2E(M)], M = \frac{4ar}{(r+a)^2 + (z-b)^2} \tag{2.1}$$

where the coil is located at $r = a, z = b$, and $K(M)$ and $E(M)$ are the complete elliptic integral functions. These are in terms of the modulus M as is MATLAB's elliptic integral function while some texts and mathematics software are in terms of the modulus k with $k^2 = M$. The rA_ϕ can then be used to plot field line location or to get the magnetic field:

$$B_z = \frac{1}{r}\frac{\partial rA_\phi}{\partial r}, B_r = \frac{1}{r}\frac{\partial rA_\phi}{\partial z} \tag{2.2}$$

The fields can be evaluated once for each set of magnets for unit current, then the final field can be found as a linear combination of the two contributing sets of magnets.

2.3.2 Calibration Equipment

To find the relation between control voltage and current in the O-coil power supply, to test the current reading on the MS-coil power supply, and to check the accuracy of the computer code, magnetic field measurements are taken of the vacuum field. Because of the slow ramp-up time of the magnetic field, pick-up loops measuring dB/dt will produce very weak signals without a large area or number of turns. The diamagnetic loops, which consist of loops around the vacuum vessel, produce a measurable response to the field, but this response is used to calibrate the loop areas and positions from the vacuum field calibration (see DML chapter). Instead calibration measurements of the field are done with Hall Effect based probes, either in the form of individual hall probe sensors, or a complete gaussmeter device.

For a bench-top check of these hall probe based systems, a small Helmholtz coil is used to provide a reference field for both DC and AC tests. The Helmholtz coil configu-

ration of the two coils approximately one radius apart gives a relatively flat field profile near the center to reduce sensitivity of probe position when calibrating. The field at the center is given by [17]:

$$B = \frac{\mu_0 n I R^2}{(R^2 + Z^2)^{3/2}} \tag{2.3}$$

for radius of coils R, distance Z apart, and with n turns in each coil. $Z \approx R/2$ for a well constructed Helmholtz coil. The coil used for calibration had 100 turns each coil, with a radius of 0.998" to 1.028", and Z of 0.501" to 0.686". This gives a center value of 1.013" and 0.594" for R and Z respectively. The coils are connected in series to ensure the same current through both.

The primary tool used for calibrating the magnetic field was a Bell 7010 gaussmeter, with an axial probe. Gaussmeter measurements on the highest DC field sensitivity at several different Helmholtz coil currents gives a field at the center of the calibration coil as $3.18 \pm 0.12 mT/A$, whereas an estimate from the geometry of the coil gives $3.14 mT/A$. Measurements at other sensitivities agreed within 0.5%, except for the 3 T range, which is used to measure the MCX vacuum field, disagreed by up to 2.8%. The calibration coil field only ranged -1.2 to 1.6 mT, due to the limits of power supply and heating of the coil. Because of this agreement, except for when covering a very small portion of the least sensitive range, the calibration of the gaussmeter is assumed to be accurate, and is used as the baseline for other magnetic measurements.

In addition to the gaussmeter, DC magnetic measurements were made with Honeywell SS94A2D hall probe sensors. These were self-contained sensors with integrated circuits to amplify, temperature compensate, and output a linear response, in a small $\tilde{1}$ cm^2 board requiring only an external DC power supply. This model was originally chosen for its quick response time of a few microseconds, but have a nominal range of only ± 0.25

T, saturating in some locations in the vacuum field. The output for zero field is half the supply voltage, with a response proportional to the supply voltage. Hence DC calibration is difficult without a known field of a size comparable to the range of the probe. DC calibration for two probes was done by placing them back-to-back in the Helmholtz coil, and measuring the difference between their outputs. This gives a measured calibration of 9.95 ± 0.2 mV/mT, with the specification for the sensor being 10 ± 0.2 mV/mT. These calibrations are for a supply voltage of 8.00 V, the default supply voltage used. Supply voltage was recorded along with Hall probe outputs during calibration and plasma shots in case supply voltage was incorrectly set.

For measurements of the field around the MCX vacuum vessel, a special holder was constructed as shown in figure 2.4. Taking inspiration from a machinist's sine bar, the rounded bottoms allow the holder to sit flat on the inside or outside of rounded surfaces of various diameters. Two holders at different z are used to hold an axial gaussmeter probe. If the two holders are made squared on flat surface beforehand, then slight wobbles are easy to notice when positioning on the curved vacuum vessel surfaces, allowing the probe to be set parallel to the vessel to within half a degree. An additional holder can be used to hold a pair of hall probes, one on the top, and one on the side to measure B_z and B_r. Due to the small size of the hall probes (0.3x0.6 inches), and use of a single holder, these may have angle errors up to 5 degrees.

2.3.3 Current Calibration

For calibration of the Eratron control voltage that determines the current through the O-coils, and scan of voltages was performed and measured by the Hall probes at $z = 65$ cm and with the gaussmeter located at $z = 163$ cm. Figure 2.5 shows the current

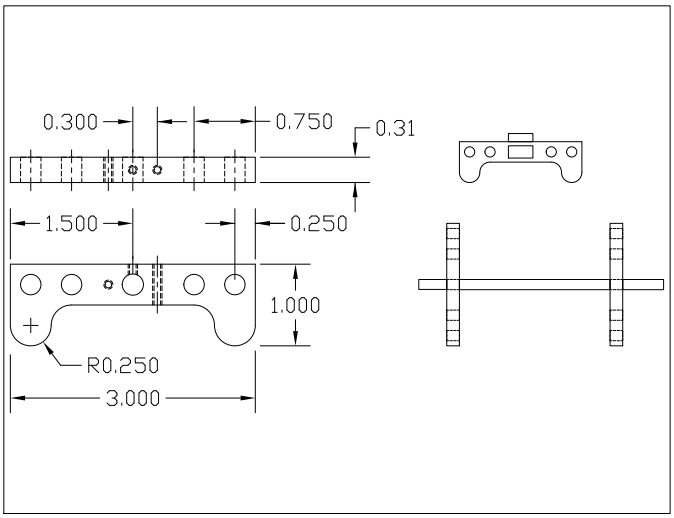

Figure 2.4: Drawing of holder for gaussmeter and hall probes, dimensions are in inches. The gaussmeter axial probe uses two such holders, being mounted in the central hole as shown in the bottom right. Additional large holes can hold threaded rods to set distance and squareness between the two holders. Hall probes are mounted on the center of the top and one side face, as seen by the two rectangles in the top right diagram.

calculated using measured field compared to the the field generating code. The B_z Hall probe and gaussmeter are in close agreement, while the B_r Hall probe disagrees slightly, by 5% at higher fields to about 10% for the lower fields. This disagreement is in part at least due to difficulty aligning the smaller Hall probes, and with B_z being about twice the size of B_r at that location, tilt will increase pick up of the z component.

As the gaussmeter is assumed to be more accurate and can be better oriented on the vessel than the Hall probes, a best fit of the gaussmeter measurements is used to calibrate the power supply. A quadratic fit gives the output current in amps in terms of the control voltage in volts as:

$$I = (37V^2 + 694V + 37) \pm 20 \tag{2.4}$$

The measured data deviates from this fit by less than 2%. At a control voltage of 4 V, the power supply was output limited, reducing current regulation ability, and the current varied with magnet temperature over at least a 5% range (this data was excluded from the above fit).

The fit found above is plotted along with an older calibration fit in figure 2.5, where $I = 848V$. A second existing, similar fit, $I = 733.5V - 117$, has also been recorded. As seen in the plot, the older fit differs from the new calibration by up to 15%. The zero intercept fit was the previously used for determining the midplane magnetic field and mirror ratio recorded in shot archives. For consistency, the fit was continued to be used in recorded data, and the labeling of mirror ratios is considered a nominal value in recorded shots (these are corrected to actual values for within this thesis). Table 2.1 shows the nominal and actual values for a few common configurations. As will be seen with DML calibration data in a later chapter, the magnetic field has not changed or drifted over several years, leaving the older fit inaccurate for all shots used in this thesis.

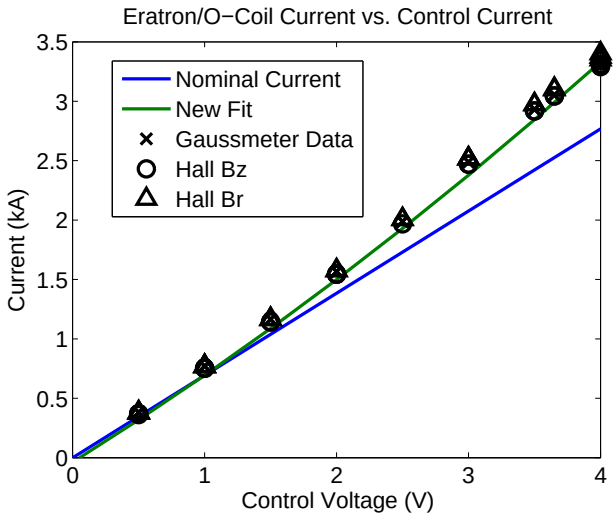

Figure 2.5: This plot shows calibration data from hall probes and gaussmeter as compared to several calibrations. The fit labeled "Nominal Fit" in blue is the calibration used for determining nominal field parameters, while the "New Fit" in green is a fit to gaussmeter data.

		Nominal			Actual			
V_{Ctrl}(V)	I_{MS}(A)	I_O(A)	R_M	B_{mid}(kG)	I_O(A)	I_{MS}(A)	R_M	B_{mid}(kG)
3.65	145	2520	7.0	2.0	3060 ± 20	148 ± 1	7.84 ± 0.07	2.16 ± 0.02
2.73	110	1890	7.0	1.5	2210 ± 20	112 ± 1	7.61 ± 0.09	1.61 ± 0.02
2.59	165	1790	5.0	2.0	2080 ± 20	169 ± 1	5.50 ± 0.06	2.10 ± 0.02
1.53	185	1060	3.0	2.0	1190 ± 20	190 ± 1	3.24 ± 0.06	2.07 ± 0.02

Table 2.1: Conversion between common nominal mirror ratios and actual mirror ratios.

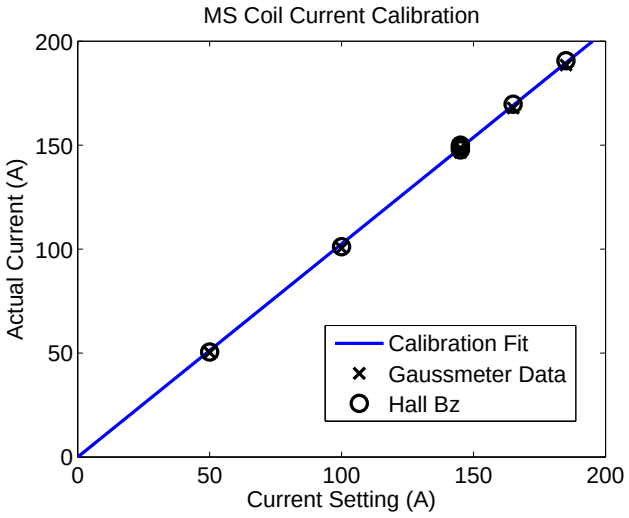

Figure 2.6: This plot shows calibration data from Hall probe and gaussmeter as compared to a calibration fit for the MS-coil power supply.

Paralleling the calibration of the current for the O-coils, a calibration of the current in the MS-coils was also performed. The MS-coils are set directly in terms of current via an analog meter readout on the power supply (set to twice the desired current desired per coil, as the pair are connected in parallel). The repeated setting by analog meter causes a variation of $\pm 1\%$ in repeatedly setting the same value. A best fit of current setting I_{set} and actual current I_{actual}, in amps, from the measured magnetic field is:

$$(I_{actual} = (1.03 I_{set} - 1) \pm 1.2 \tag{2.5}$$

Figure 2.6 shows the fit vs. gaussmeter and Hall probe measurements. The fit and data disagree by less than 2%.

Both calibrations of magnet coils above assume the code faithfully reproduces magnetic geometry. A scan of magnetic field measurements along z shows agreement with the field shape measurements once the above calibrations have been made. Figure 2.7 shows measurements along z for the O-coil field. The maximum deviation is 4-5% near the cen-

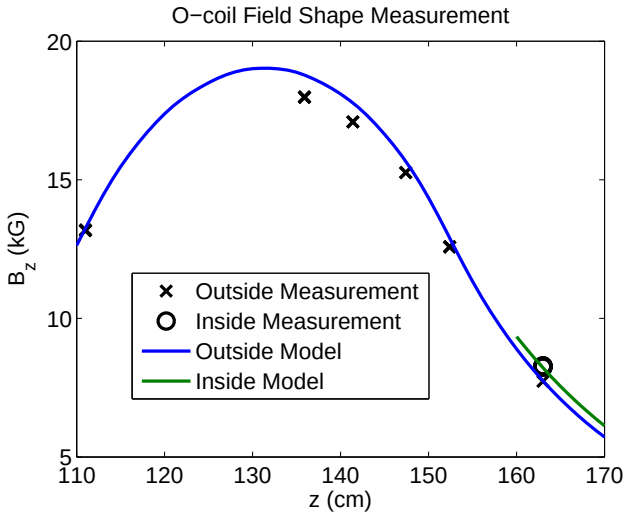

Figure 2.7: A plot of measurements of magnetic field along z testing the shape of the O-coil's field produced by magnetic field modeling code. Outside measurements were taken outside, along the surface of the vacuum vessel, while inside measurements were taken inside the vacuum vessel. The model results are displayed separately for these two different radii, with the inside model results shown just near the inside measurement.

ter of the coil. This is where the details of the layout of the coil's turns are expected to matter most; hence, due to uncertainty in the positions of these turns, this slight deviation centered there is expected. Similarly in figure 2.8, measurements along z for the MS-coil show agreement within 2.5%.

Azimuthal symmetry was checked and found to be less than $\pm 1\%$ variation for the O-coil, and less than $\pm 0.5\%$ for the MS-coil fields. Symmetry across the midplane has been found to be within 2%.

2.3.4 AC Field Component

The O-coils exhibit a complicated AC noise on top of the DC field, with the waveform shown in figure 2.9. These oscillations are only on the order of 6-8 mT at the measured locations, which are about 0.5% of the DC vacuum field. The waveform consists

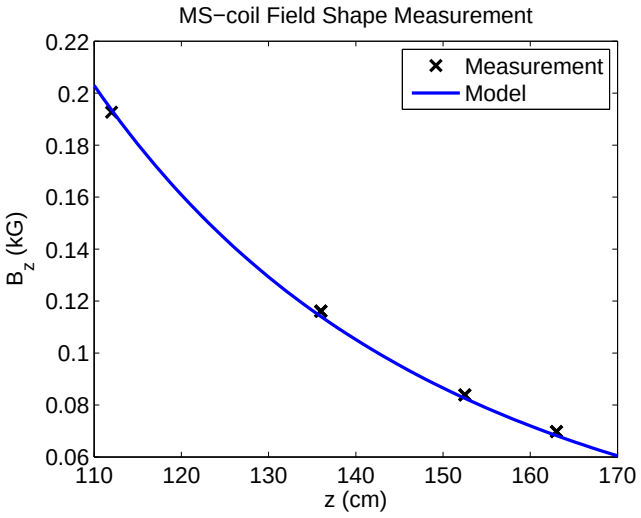

Figure 2.8: A plot of measurements of magnetic field along z to test the shape of the MS-coil's field produced by magnetic modeling code. Measurements were taken along the outside surface of the vacuum vessel.

of harmonics of 60 Hz, with the dominant frequency of 360 Hz followed by 60 Hz. This suggests the noise is from the rectification of AC in the power supply. While small compared to the magnitude of the DC component, these oscillations are comparable in size to some magnetic measurements from the plasma.

With typical plasma durations of 5 ms, a 60 Hz pattern would only complete a portion of the cycle, with arbitrary phase since the plasma is not triggered in sync with the mains frequency. This complicates measurements based on $\frac{dB}{dt}$ from the arbitrary start in the cycle. However, the AC component drops off faster in z than the DC component, so this would only affect measurements close the O-coil. The chapter on DMLs go into more detail about the z dependence of this effect.

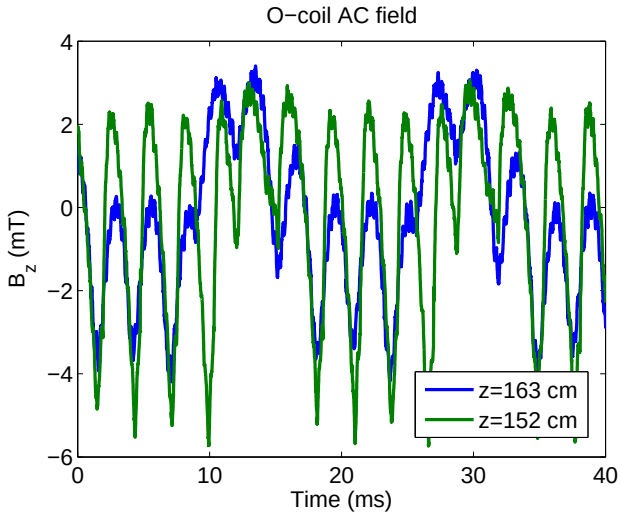

Figure 2.9: AC noise in field of the O-coil measured at two different z locations. Both measurements were taken outside the vacuum vessels. Measurements inside the vessel at $z = 163$ cm look identical to outside measurements plotted above.

2.3.5 Mirror Ratios

The significance of the mirror ratios 7.8 and 3.2 are their contrasting field line shape as shown in figure 2.10.

Mirror ratio 7.8 is the more typical operating condition for MCX, which is close to the highest mirror ratio possible with a midplane field of 2.1 kG. The field lines have a minimum at the midplane, hence plasma would be expected to be confined to the axial center of the machine.

Mirror ratio 3.2 has a qualitively different shape as a result of the positioning of magnet coils. Instead of a minimum at the midplane, there are two minima located off-midplane near the first jog in the vacuum vessel. Plasma would be expected to concentrate off-midplane, in two places analoguous to running two MCX-like machines in tandem. This contrast gives provides an extra test of diagnostics.

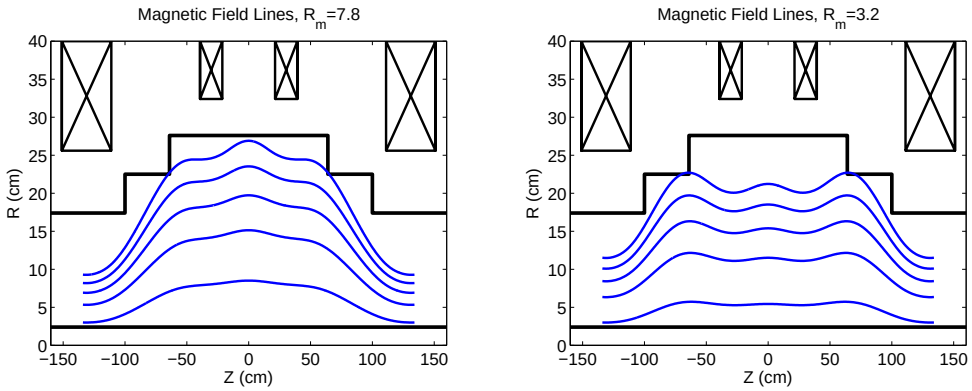

Figure 2.10: These plots show field lines between the LGFSes for two mirror ratios used frequently in this thesis. The vacuum vessel, core, and magnet coils are shown in black.

2.4 Vacuum Pumping and Cleaning

The vacuum for the experiment is prepared by two stages: a mechanical roughing pump and a turbomolecular pump. Originally the mechanical roughing stage used a rotary pump. This pump was later replaced with a oil-free mechanical scroll pump as part of a campaign to improve the vacuum and reduce contamination of the plasma. Along with additional methanol based cleaning of the interior of the vacuum chamber, this effort showed a continuing decrease in the presence of carbon within the machine as seen by spectroscopic lines.

Additionally cleaning via helium glow discharge was attempted, which showed reduction in water within the machine after pumping down from a vacuum break. However, the normal plasma discharges produce similar cleaning effects, so the first few discharges of the day make the discharge cleaning mostly redundant. Similarly, heating/baking of the vessel can reduce water content, but the effectiveness was not deemed enough to warrant the space required by the heating blankets (such as in the tight space between the

vessel and the inner magnet coil sets) or the replacement of some temperature sensitive diagnostics and components.

2.5 Capacitor Bank

To both provide the voltage for breakdown and the electric field between the core and the vacuum vessel, a bank of capacitors is charged and then quickly connected to the core via an ignitron based switch. The bank consists of 32, $60 \pm 5\mu$F capacitors in parallel for a total capacitance of 2 mF, rated up to 20 kV.

An equally sized second bank of capacitors could be connected in parallel, independently switched; however, this was rarely used. This second bank was later deconstructed and rebuilt with a new layout with the intent to increase safety and maintainability, along with new safety procedures, which are documented below as pre-existing documentation of such is light.

The original layout placed the capacitors in an upright position, with terminals pointed upward, on two levels of wooden shelves. The terminals were connected to high voltage coax cable via brass brackets. There were a pair of coax cables in parallel for each capacitor, which were then routed and combined at a single point. The large amount of cabling used, combined with Mylar sheets wrapped around various parts of the terminals to reduce chances of arcing, the height of the second shelf, and the limited head space above the capacitors, all greatly reduced visibility and access to the terminals. Additionally, the cabling applied stress to a soldered join on the brass brackets which became susceptible to mechanical failure. At least one such failure occurred during charging of the capacitors, leaving a charged capacitor disconnected from discharging and bleeding circuits while being a difficult fault to find due to obstructed visibility of capacitor connections.

The new layout arranged the capacitors on their side, in an array of eight wide and four high, each supported by aluminum scaffolding. The coax cables and brass brackets were replaced by copper bus bars directly bolted to the terminals of the capacitors in groups of four [18]. Coax cable was only used to connect the ends of each set of bus bars together, and tightly wrapped Mylar was only used where the high voltage bus bars passed close to the aluminum scaffolding. This allowed visibility and easy access to all of the connections and terminals.

Additionally, new safety procedures were added to confirm the discharged state of the capacitor bank after use. Previously the bank was only discharged through a normally-closed switch that closed after each discharge, interlock opening, or power failure, and through a second discharge switch engaged during maintenance. The new procedure was applied at the end of a day of use or when personnel expected to be in the vicinity of the bank. First each set of bus bars was checked with a high voltage probe and voltmeter, while wearing hearing protection, high voltage gloves, and arc flash face shield. Once all voltages were confirmed to be zero, each set of bus bars was shorted by a set of clamped cables, and finally a grounding hook was attached to a central point. If the voltages were ever found to not be zero, indicating failure to discharge, the capacitors could easily be individually discharged by grounding through a high power resistor attached to a nonconducting handle.

One consideration during the development of this procedure was potential arc flash from a discharge of the banks. The flash of electrical discharges can contain a large amount of UV light and carry enough energy to produce serious burns in larger discharges. Arc flash is accessed in terms of cal/cm^2 of energy, typically at a distance of 18 inches from an arc. Safety standards, such as the NFPA 70E [19] concentrate evaluations of arc

flash sources on discharges sourced from AC mains that can supply a constant power at high fault currents until interrupted. Formularies in this standard are also only valid for discharges up to 600 V. Instead, an upper bound can be found by dividing the full energy of a charged capacitor, $\frac{1}{2}CV^2$, by surface area of a hemisphere, assuming half of the flash is reflected by the bank or other surface behind it. This gives an upper bound of arc flash energy density of 0.2 cal/cm ^{2} for a single capacitor or 7 cal/cm^2 for the whole bank, at a full charge of 20 kV. Onset of second degree burns is given as 1.2 cal/cm^2 in such standards, and energy densities below this are in the lowest category not requiring special protective gear. This suggests keeping a distance of at least 4 ft from energized equipment when the whole bank could be charged to keep potential exposure below 1.2 cal/cm^2. During safing of the bank, the arc flash would not be an issue if a single capacitor or row of capacitors were still charged due to a single connection failure.

Additional concerns included the forces upon the bus bars due to adjacent currents [20]. In the case of the capacitors being discharged through a low series resistance of 1 Ω at full charge, a peak current of 20kA will be distributed across eight sets of busbars. With lengths of about 1.5 m, and separation of about 15 cm, this works out to a force of 13 N. This force is considered acceptable based on the mechanical rigidity of the setup, and is larger than the typical 0.8 N that would be seen discharging the bank at half charge through a 2 Ohm series resistor, or a quarter that for typical plasma currents.

2.6 Other Electrical Components

There are two switches, both ignitron type mercury switches: one to connect the bank to the core, and a “crowbar” switch that shorts the core and capacitor bank. The latter is used to end a shot at a predetermined time to examine the afterglow and spin

down of the plasma.

Current into and out of the core is measured with a commercial Pearson current monitor right at the vacuum feed through. Older shots used a hand made Rogowski coil. These shots can be distinguished by older monitor shots having a "Plasma Current" data acquisition channel and shots with the new monitor having a "New Plasma Current" channel. Older monitor shots have already converted to kiloamp units, while the newer one is recorded in volts with a factor of 2 kA / V (combined factor for monitor and an attenuator). The voltage is measured using a 65kΩ:25Ω=2600:1 voltage divider, and automatically converted to kV when recorded by the data acquisition system.

Data acquisition (DAQ) is done on a National Instruments S-series data acquisition system using PXI-6133 analog to 14-bit digital converters. The channels can be set to either single ended, referencing signal to the DAQ ground, or differential mode. Older shots were recorded at 1 megasamples / second, while newer shots tended to use maximum speed of 2.5 megasamples / second.

Chapter 3

Interferometer

MCX operates two IR interferometers for measurement of plasma density that were constructed previous to the author's research, with the operation and maintenance later assumed by the author. This chapter discusses the design, operation and results of these interferometers.

3.1 Basic Principles

From the dispersion relation for electromagnetic waves in a plasma, $\omega^2 = \omega_p^2 + k^2c^2$, the index of refraction can be found as [21]:

$$n = \frac{ck}{\omega} = \sqrt{1 - \frac{\omega_p^2}{\omega}} \approx 1 - \frac{\omega_p^2}{2\omega^2}$$

Because this is less than one for $\omega > \omega_p$, light going through a plasma will have slower phase velocity compared to light in a vacuum and experience a relative phase shift compared to a second beam avoiding the plasma. Because of the plasma density dependence of ω_p, a measurement of such a phase shift can provide a measurement of the plasma density transversed by the beam. With $\Delta t = \Delta\theta/\omega$ and $\Delta t = l/v = l\Delta n/c$, the relative difference in phase θ and timing t over a path length l for a relative difference in index of refraction Δn:

$$n_e = \frac{2\Delta\theta c m_e \epsilon_0 \omega}{le^2}$$

For a non-uniform density over the path length, the measured density is an average of the density along the path. Hence the basic principle of using an interferometer to measure

the average electron density: compare the phase of a light beam going through the plasma of interest to a reference beam.

As optical frequencies are too high to directly observe, the plasma beam and reference beam are optically combined/superimposed and the resulting intensity is measured to find the difference in phase of the two beams. In a homodyne interferometer configuration, where the reference beam and plasma beams are identical other than path, the intensity measured by the detector would be proportional to $\cos \Delta\theta$. This presents a problem at a phase difference of 0 and 180 degrees, where there is no sensitivity to changes in phase, reducing accuracy close to these phase differences and, more importantly, a lack of ability to tell the sign of following phase changes. This is solved by a heterodyne configuration [22], where the reference beam is modulated with a frequency ω_0, and the detector measurement becomes proportional to $\cos \omega_0 t + \Delta\theta$, removing the lack of accuracy at certain phase differences. The reference and plasma beams are mixed optically to produce a ω_0 signal on the detector, which can then be phase compared electronically with the original ω_0 signal to yield the accumulated phase difference $\Delta\theta$.

3.2 Equipment

There are two interferometer setups on the machine. One is located at the midplane, $z = 0$, but passes through offset from the center line by 15.5 cm. The second, transition region interferometer is located at $z = 91.5$ cm from midplane, and with an offset of 5.75 cm from the centerline. The two interferometers are nearly identical otherwise, with the exception of an additional visible light laser on the midplane interferometer (described below) and the transition interferometer using a convex lens to focus both beams onto the detector whereas the midplane interferometer only has such a lens on the plasma beam.

The main parameter choice in a setup is the ω of the light beams being used. The smaller the ω, the larger the phase change induced by a given density and hence the larger the accuracy of measurements. However, as ω approaches the plasma frequency, attenuation and nonlinear effects become significant. The typical MCX plasma frequency corresponds to a wavelength of light of 0.2-0.5 mm. The resulting operating frequency chosen with these criteria in mind and the availability of related equipment was 3.39 μm.

This frequency of light was generated by a helium-neon laser. While more commonly known for their bright 633 nm red transition, a helium-neon laser incorporating an appropriate filter and mirrors can generate the 3.39 μm transition. The lasers used were 2 mW in power at this wavelength (whereas a similar HeNe laser used for the 633 nm was 12 mW in power).

The choice of the ω_0 parameter needs to be such that it is faster than the expected evolution of density in the plasma to avoid the ambiguity found at the 0 and 180 degree phase shifts. To be faster than the rotation time scale of around 100-200 kHz, ω_0 would need to be in the megahertz range. Modulation in this range can be achieved by a Bragg cell, an optoacoustic coupler that sets up a standing sound wave in a crystal of the desired modulation frequency. The sound wave creates a regular pattern of variation in the index of refraction, diffracting an incoming light beam and imposing the modulation upon the diffracted beam. The cell also allows some light through undiffracted, acting as a beam splitter for the plasma and reference beam at the same time as modulating the reference beam. For the MCX interferometers, a modulation of $\omega_0 = 40$ MHz was used.

The optics of the interferometers are in a Mach-Zehnder configuration, containing a separate beam splitter for splitting and mixing the beams (the former being the Bragg cell). The plasma beam passes through the vacuum vessel and plasma via windows, reflects

off a retroreflector, then retraces nearly the same path through the plasma. The plasma and reference beams are of different path lengths, but this is inconsequential as only a relative phase shift is needed at any moment as compared to the phase observed before the plasma formation.

The midplane interferometer also contains a visible light HeNe laser. With a shorter wavelength, this laser would be less sensitive to plasma density, but more sensitive to vibrations in the optics and could be used colinearly with the IR laser to measure and compensate for vibration within the setup. However, this compensation was found to be unnecessary and the visible laser remains as an aid for aligning optics of the invisible IR laser.

The comparison of the phases between the reference RF signal and the optical mixed output of the interferometer is done by an electronic phase comparator which outputs two voltages that correspond to the x and y of a point on a circle with an angle equal to the phase difference. In other words, the phase difference comes from recording these two signals, and taking the arctangent. The received signals can be quite weak, on the order of a few tens of millivolts. The weak signal combined with the arctangent operation can produce a large amount of high frequency noise on the calculated phase difference. This noise is reduced by applying a window filter to the two recorded x and y signals before applying the arctangent. Typically a window of about 100 samples (0.1 ms for 1 MS/s sampling rate) is used to filter out the noise at the expense of averaging out and reducing signals on a shorter timescale. Also, software must remove large, sudden jumps of the phase signal, typically with a threshold of $3\pi/2$, to account for the phase angle moving over the π to $-\pi$ discontinuity.

3.3 Operation and Calibration

Under normal conditions the operation of the interferometers can become a turn-key operation, where the equipment needs to only be turned on and the output recorded by the data acquisition system. However the alignment of various components needs to be corrected or restored from time to time, experiencing degrading on timescales from days to months, or after equipment is bumped. The largest source of the misalignment is due to the location of retroreflectors on seperate stands disconnect from the optical table containing the rest of the optics. These retroreflectos are mounted on vibration reduction platforms, but still are able to move and vibrate independantly from the rest of the optics.

The alignment consists of two portions: a coarse and fine alignment. The coarse alignment involves maximizing the DC signal seen by the detector for each of the two beams individually (i.e. blocking the other beam). If the beam doesn't reach the detector, a spare detector can be used to locate the beam. Once each of the beams' DC component has been maximized onto the detector, finer adjustment is done when observing the AC component, maximizing the ω_0 modulation signal seen at the detector with the two beams mixing. An oscilloscope with a FFT feature greatly eases the isolation of the ω_0 component from other higher and lower frequencies that exist from laser modes and other sources of noise.

A previously performed calibration and check for the operation of the interferometer is to measure the index of refraction of air. As the interferometer measures relative change in phase, the index for air is measured by recording the phase difference from flooding the pumped down vacuum vessel with atmospheric pressure air (done quickly, to avoid errors from the phase drifting over time from other sources). In this case, the phase difference

seen would be:

$$\Delta\theta = \frac{2\pi l \Delta n}{\lambda}$$

This corresponds to a phase shift of about 586 radians at normal atmospheric pressure and 30 C (or about 93 full fringes).

Additionally, another simple test of calibration is to model the plasma as a capacitor that stores energy as rotational kinetic energy while running, and releases that energy when the shot is ended by shorting out the plasma (as was done in [23]). After the crowbar switch is closed at the end of the shot, plasma current is seen to switch from flowing into the plasma to out of the plasma. The energy returned during this current reversal corresponds to the density and rotation velocity (estimated from plasma voltage) at the end of the shot.

3.4 Noise Sources

For comparison to the effects of prefill conditions during a plasma shot, hydrogen's Δn is roughly half that of air at the same pressure, and scales with pressure. At a typical prefill pressure of 5 mTorr, the prefill would produce a shift of 0.002 radians, corresponding to a plasma density of about $2 \times 10^{17} m^{-3}$, two orders of magnitude below the noise floor of the interferometer. Additionally, since this prefill exists at the start of data acquisition, its effect would not be seen by the relative measurement of the phase. Although what the prefill pressure does on the timescale of the plasma shot is unknown, so this would serve as an upper bound on the effects of the neutral prefill on density measurements.

Besides changes in phase due to changes in plasma density, vibration and instabilities in the laser source can cause additional shifts. Monitoring the phase over a long time period, as shown in figure 3.1, show sinusoidal drifts. The dominant frequencies are

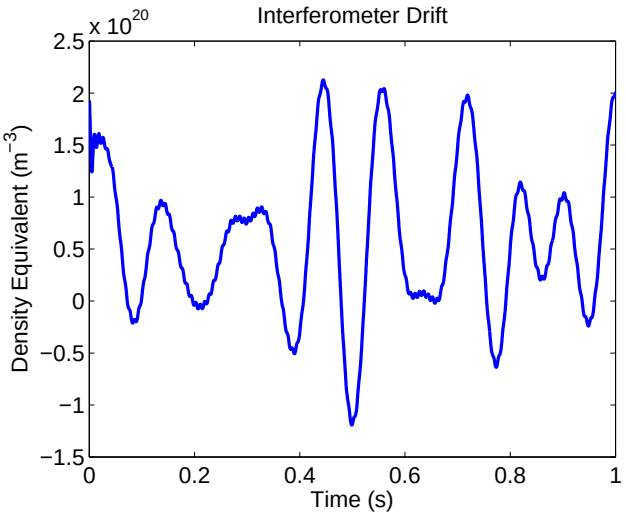

Figure 3.1: Plotted here is an example of phase drift on an interferometer over time scales much longer than a typical plasma discharge.

roughly 7 Hz and 120 Hz, with amplitudes, in terms of equivalent density measurement, of $4 \times 10^{20}\mathrm{m}^{-3}$ and $5 \times 10^{18}\mathrm{m}^{-3}$ respectively. Over the course of a 10 ms shot, low frequencies like the 7 Hz noise appear as a near linear background, and can be subtracted out. The linear background can be found from either looking at the slope in the 0.5 ms recorded before breakdown, or by looking at slope across the whole 10 ms shot. The latter is found to yield lower error for sinusoidal background. Using this method gives errors from a pure 7 Hz and 120 Hz backgrounds of $5 \times 10^{18}\mathrm{m}^{-3}$ and $9 \times 10^{18}\mathrm{m}^{-3}$respectively.

3.5 Definition of Path Length

Since the measured density is averaged over the path length, the exact definition of the path length used is important. Path length in calculations of the interferometers used on MCX are in terms of the distance traveled within the LGFS as calculated for the vacuum field, as opposed to distance within the vacuum vessel or within some constant

radius. This means the path length will vary with mirror ratio. For example, the total path lengths, including both passes, for mirror ratio 7 are 81.9 cm and 55.6 cm for the midplane and offset interferometers respectively, while 54.6 cm and 68.3 cm for mirror ratio 3.

Besides using the full magnetic field calculations to estimate these path lengths, the following polynomial fits are accurate to within 0.7% over the range of $2 \leq R_m \leq 14$ giving the path length in centimeters:

$$l_{mid} = 29.93 + 10.06R_m - 0.313R_m^2 \quad l_{tran} = 99.56 - 14.77R_m + 1.716R_m^2 - 0.715R_m^3 \quad R_m \leq 8.8$$

$$l_{mid} = 91.36 \qquad\qquad l_{tran} = 117.2 - 10.01R_m + 0.319R_m^2 \qquad R_m \geq 8.8$$

The change at $R_m = 8.8$ is due to the LGFS switching between hitting the step in the vacuum vessel at $z = 65$ cm and midplane, where in the latter case the radius is constant for higher mirror ratios at the midplane.

3.6 Density Results

For most discharges, the midplane interferometer will record a quick rise in density on the time scale of 0.5-1.0 ms from breakdown, and then a gradual drop-off over the course of the discharge. For the common mirror ratio 7, peak densities of $2-4\times10^{20}m^{-3}$ are seen, with a drop-off of about 50% over the remaining 4 ms. The off-midplane interferometer measures very low densities on the order of $1 \times 10^{19}m^{-3}$, often close to noise thresholds ($0.5 - 2 \times 10^{19}m^{-3}$ depending on the shot and quality of alignment at the time), for high mirror ratios like 7. A typical mirror ratio 7 shot is shown in figure 3.2. Hence there is a very large accumulation of density near the midplane compared to the transition area. Additionally, after the end of the discharge when the plasma is shorted, while the midplane density shows a decay, the transition density will show a short increase for 0.5-1 ms before

decaying. This suggests that plasma confined to around the midplane is released upon stopping the discharge and is seen flowing past the off-midplane interferometer as the plasma expands.

When a lower mirror ratio of 3 is used, there is a large change seen in the ratio of the two density measurements. While at mirror ratio 7 the midplane density was seen to be up to 30 times larger than the transition density, at mirror ratio 3 the midplane density can be 30-70% of the transition. In other words, the transition density is 1.5-3 times larger than the midplane density for mirror ratio 3. For the mirror ratio 3 shot plotted in figure 3.2, the midplane peaks at about $5 \times 10^{19} m^{-3}$ and starts to drop-off while the off-midplane shows a near constant $1 \times 10^{20} m^{-3}$ density. The ratios of pressures versus time are plotted for several other mirror ratios in figure 3.3 while figure 3.4 displays just the ratio of densities averaged over a 1 ms time interval. The midplane to transition ratio of time averaged density ranges from 20-30 for $R_m = 7$ and 7-15 for $R_m = 6$, while transition to midplane ratios are seen from 1-1.5 for $R_m = 4$, 1.5-3 for $R_m = 3$ and 5-13 for $R_m = 2$.

Over the course of the discharges the phase shift of the interferometer drifts for reasons other than the plasma, such as vibration or thermal expansion affecting the distance between optics. In the plots such as figure 3.2 a linear component is removed from the density trace, i.e. a linear function is subtracted such that the first and last densities of the trace are forced to zero. Otherwise, the traces would end up slightly off of zero at $t = 10$ ms when the plasma has dissipated enough to leave nearly zero density left. For the shots from MCX090604-14 to -27 used for those plots, the average of the absolute value of the deviation at the end was $2.5 \pm 2.5 \times 10^{19} m^{-3}$ for the midplane, and $2.9 \pm 4.4 \times 10^{19} m^{-3}$ for the transition. These offsets can vary from day to day as the sensitivity to noise varies for

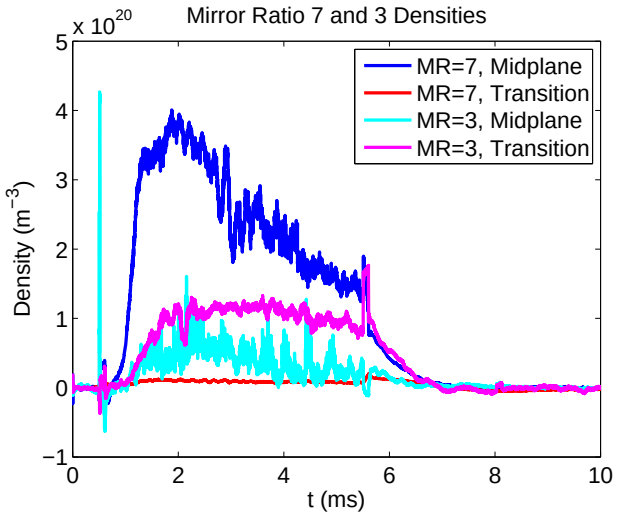

Figure 3.2: Two typical shots, MCX090604-14 and -23, one mirror ratio 7 and the other 3, showing the two density measurements with respect to time. The two shades of blue show the midplane measurement, and the two shades of red show off-midplane measurement.

the interferometer. A large component of this may be due to the mounting and balancing of the retroreflector, which not being on the optical table with the rest of the components, could be subject to larger movements and vibrations even though it is placed on an anti-vibration stand. Once the linear component is removed, there may still be shift over the course of the shot, however looking at the time from 7.5 ms to 8.5 ms shows a shift of only $4 \pm 3 \times 10^{18} m^{-3}$ and $5 \pm 4 \times 10^{18} m^{-3}$ suggesting the largest part of the shift has been removed.

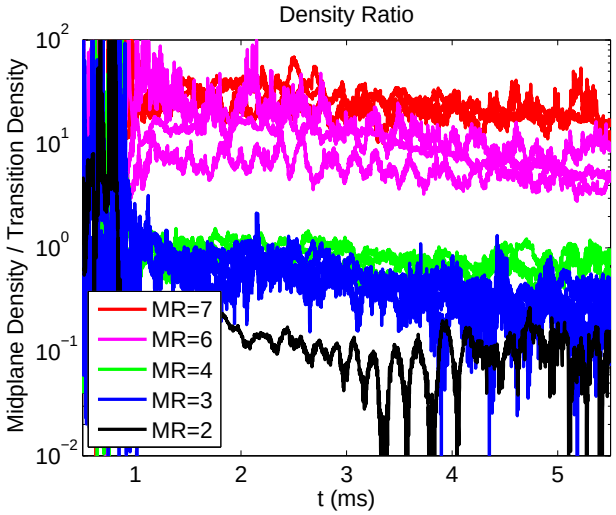

Figure 3.3: Showing the density ratio, ρ_{mid}/ρ_{tran}, for shots MCX090604-14 to -27 which cover several mirror ratios. The y-axis is log scale to show both high and low ratios.

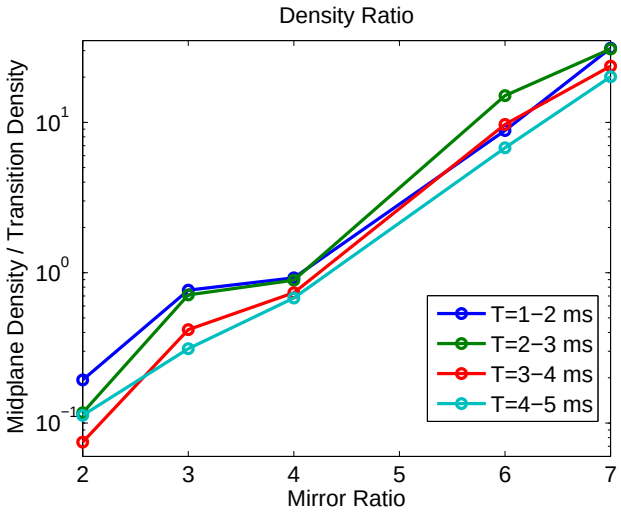

Figure 3.4: Showing the density ratio, ρ_{mid}/ρ_{tran}, for same shots as in 3.3. Instead here the ratios are plotted for versus mirror ratio, using an average over a 1 ms period, taken at several different times, for each mirror ratio.

Chapter 4

Spectrometer

This chapter discusses the use of Doppler spectroscopy to measure velocity and temperature profiles of the plasma, including the analysis required to extract radial profiles from chord based measurement of impurity lines.

4.1 Basic Principles

With a temperature over several eV, collisions within the plasma easily excite electrons within neutral atoms and ions within the vacuum vessel, resulting in the emission of atomic transition lines. As the wavelengths of these transition lines are well tabulated, comparison between observed wavelength and tabulated wavelength can yield the velocity of the emitting ion/atom via the Doppler shift in wavelength:

$$\Delta\lambda = \lambda_0 \frac{v}{c} \tag{4.1}$$

with the higher order $\mathcal{O}(v^2/c^2)$ terms dropped as velocities are non-relativistic in the MCX plasma. The ions in the plasma have both a bulk velocity and thermal velocity. For the latter, convoluting the Doppler shift with a Maxwellian velocity distribution results in a Gaussian profile of wavelengths. While the mean shift of the distribution gives the average velocity, for a Gaussian distribution expressed as $\frac{1}{\sigma\sqrt{2\pi}} \exp(-\frac{(\lambda-\lambda_0)^2}{2\sigma^2})$, the ion temperature can be extracted from [24]:

$$\sigma = \sqrt{\frac{kT}{mc^2}}\lambda_0 \tag{4.2}$$

However other effects can contribute to broadening and shifts. The Stark effect can

broaden and shift lines from electric fields, including a pressure broadening effect due to interaction between an ion and the electric fields of passing electrons and ions. Stark broadening for various carbon, nitrogen, and oxygen lines that are typically examined on MCX show broadening (FWHM) widths on the order of 0.02 nm for electron densities of $10^{22}\mathrm{m}^{-3}$ or more [25]. This requires densities more than a factor 10 larger than peak MCX densities, and at the threshold of resolution of the spectrometer used before taking other broadening effects into consideration. Stark shifts are on less than 0.01 nm for the same pressures, and likewise below the spectrometer resolutions. Hence the Stark effect is disregarded.

Spectral lines could additionally be broadened by turbulence. If there are variations in velocity on the order of thermal velocities within the spectrometer's view, the emitted spectral lines could have additional broadening. As a result, ion temperature measurements are to be interpreted as upper bounds on ion temperature if there is uncertainty in the amount of turbulence within the plasma.

4.2 Impurity Velocities

If one considers the neutral density outside the plasma to be on the order of the hydrogen prefill, about $1.5 \times 10^{20} m^{-3}$, then an ion-neutral collision frequency of 100-200 kHz would be expected for ion velocities comparable to the 10-50 eV thermal velocity. Hence the mean free path of a hydrogen neutral would be on the order of a centimeter, much smaller than the typical 20 cm between inner and outer LGFS at midplane (which is comparable to the electron-ion mean free path near the edge of the plasma, as opposed to the electron-ion mean free path closer to 20 cm at peak temperature and rotation in the center of the plasma). Hence, direct spectroscopic observation of bulk hydrogen plasma is

not possible under most conditions due to the high degree of ionization of plasma. Also, the electron-ion mean free path is shorter than the parallel length, thus validating the use of isotropic pressure in the MHD equations presented later.

Observation of spectral lines within the plasma, especially the densest, central portions, must instead be based on impurity lines. To the lowest order, the measurements of velocities for the impurities may be assumed to be representative of the hydrogen bulk plasma, as the $\mathbf{E} \times \mathbf{B}$ drift velocity is independent of mass and charge: $|v| = |E|/|B|$. Additionally, curvature and $\nabla \mathbf{B}$ drifts are on the order of a few m/s compared to the tens of km/s rotation speeds. However, within a cylindrical configuration with radial electric field, this form of the drift velocity is only the lowest order approximation.

One approach to deriving the $\mathbf{E} \times \mathbf{B}$ drift velocity is to boost to a frame such that the electric field is zero, giving a frame where the particle gyrates, but doesn't drift, and hence giving the drift velocity. Likewise, transforming to a rotating frame with a velocity such that the transformed electric field balances the centrifugal force (taking into account $\mathbf{E}$ points towards core for typical operation):

$$\begin{aligned}
q\mathbf{E}' &= -m\omega^2\mathbf{r} \\
q(E - vB) &= m\frac{v^2}{r} \\
mv^2 + qrBv - qrE &= 0 \\
|v| &= \frac{qrB}{2m}\left(1 \pm \sqrt{1 + \frac{4Em}{qrB^2}}\right) \\
&\approx \frac{qrB}{2m}\left(1 \pm \left[1 + \frac{2Em}{qrB^2} - \frac{2E^2m^2}{q^2r^2B^4} + \mathcal{O}\left(\frac{E^3m^3}{q^3r^3B^6}\right)\right]\right) \\
&= \frac{E}{B} - \frac{E^2m}{qrB^3} + \mathcal{O}\left(\frac{E^3m^2}{q^2r^2B^3}\right) \\
&= v_0\left(1 - \frac{v_0}{\omega_c r} + \mathcal{O}\left(\left[\frac{v_0}{\omega_c r}\right]^2\right)\right)
\end{aligned}$$

Here $v_0 = E/B$ is the lowest order $\mathbf{E} \times \mathbf{B}$ drift velocity typically used for estimating

rotation velocity. The other, dropped solution of the quadratic equation gives the case of cyclotron motion centered on the core. For a rotation velocity of 100 km/s at a radius of 20 cm, the next order correction works out to only 2.6% for hydrogen, while for doubly ionized carbon this gives a 16% correction in rotation velocity.

Additionally, the electric field is not constant over the entire cyclotron motion within this frame, due to slight changes in angle of the electric field. The deviating angle is $\rho_L/2\pi r = \sqrt{Tm}/2\pi qBr$. Even a typical field minimum of 2 kG and a temperature of 100 eV gives a variation of the electric field of 0.4% (in the rotation direction) over the cyclotron motion for hydrogen, and 0.7% for doubly ionized carbon.

4.3 Deconvolution

The spectra from the plasma are observed not from a single point, but along a line, giving an integration of all light along that path. Thus, to observe spectra from the inner portions of the plasma, light from the outer portions will be seen within the same view as all spectra are recorded from the outside of the plasma. By assuming cylindrical symmetry, results from multiple chords can be combined to measure the emissions by the outer portions of plasma, and remove their contributions to views of the inner portions of plasma.

The Abel inversion is a simple version of such a process for obtaining a radial profile of light intensity from measurements of chords spaced out with different impact parameters b (the minimum distance between the chord and central axis). The plasma is assumed to be cylindrically symmetric, and is divided into concentric layers such that each layer extends from one impact parameter of an observation chord to the next largest impact parameter. Each layer is then assumed to be homogeneous. For this intro, only intensity

of light is assumed to vary between layers. The chords and layers are numbered from the outside to inside, with 1 being the outermost. Then the intensity emitted per linear unit by the outer layer, I_1, can be found directly from the outermost observed intensity, O_1:

$$I_1 = \frac{O_1}{l_{l,l}} \tag{4.3}$$

Here $l_{1,1}$ is the path length of chord 1 through layer one. The lengths can be found from:

$$l_{1,1} = 2\sqrt{r_{max}^2 - b_1^2} \tag{4.4}$$

$$l_{i,1} = 2\sqrt{r_{max}^2 - b_i^2} - l_{i,2} \tag{4.5}$$

$$l_{i,j} = 2\sqrt{b_{i-1}^2 - b_i^2} - l_{i,j+1} \tag{4.6}$$

$$l_{i,i} = 2\sqrt{b_{i-1}^2 - b_i^2} \tag{4.7}$$

where r_{max} is the outermost radius of the outer layer (the maximum radius considered for light emission). Now with the intensity of the outer layer known, and with the path length of the second chord through the outermost layer, $l_{2,1}$, the emissions from the outer layer can be subtracted to yield the intensity density of the inner chord:

$$I_2 = \frac{O_2 - O_1 l_{2,1}}{l_{2,2}} \tag{4.8}$$

And likewise the process peels outer layers off of other chords to give the intensity density for each layer as:

$$I_i = \frac{1}{l_{i,i}} \left(O_i - \sum_{k=1}^{i-1} O_k l_{i,k} \right) \tag{4.9}$$

While this process can be directly applied when each layer varies only in intensity, the plasma within MCX varies by intensity, temperature, and velocity radially. If not for the Doppler velocity shift, the above process could just be repeated for each wavelength separately. However, even with a constant velocity for a a given layer, each chord intersects

that layer at a different angle introducing a cosine factor. This requires outer layers to be shifted and adjusted in intensity before removing them from views of inner layers.

There are three different methods of modeling the velocity and temperature seen by each chord. The first method is to find the center of mass of a peak (and hence will be referred to as Center of Mass, CoM, method), and use this as the Doppler shifted position. Temperature is then found from the full-width half-max of the peak. Then the whole spectrum can be shifted and scaled as needed before subtracting from more inward chords. This method does not make assumptions about the exact shape of the peak for deconvolution purposes (still assumes Gaussian shape to get temperature from FWHM), only assuming that temperature and velocity are constant within each layer.

A second method is to assume each layer has uniform temperature and velocity, and to fit a Gaussian curve to each deconvoluted chord to yield a velocity and temperature. A Gaussian that has been scaled and shifted is then subtracted from each chord when deconvoluting. This will be referred to as the step method, as it assumes a step profile for velocity and temperature.

Finally, the various profiles can be assumed to be piecewise linear, such that they smoothly vary from layer to layer. The resulting spectrum seen for each chord is not an exact Gaussian, but can be generated numerically by summing the spectra across many points along the chord:

$$O_i(\lambda) = \sum_j I(\lambda, r_{ij}) \exp\left(-\frac{(\lambda - \lambda_0(r_{ij}))^2}{2\sigma(\lambda, r_{ij})}\right) \tag{4.10}$$

The points r_{ij} should be evenly spaced along the length of chord i, not evenly spaced radially. This can be fitted to the observed spectra by minimizing square residues. The minimizing can be performed by considering all of the chords together or, to minimize the number of variables being fitted at a time, each chord can be used to fit only the next

portion of the profiles. This last method, using the latter minimization process, will be referred to as the piecewise linear method.

To compare these methods, simulated observations can be created, using equation (4.10) as with the piecewise linear method, but using different, non-piecewise-linear profiles. Values similar to those previously seen in MCX plasmas can be used for peak values of profiles, 100 km/s and 20 eV. Likewise, parameters of the actual spectrometer can be used: 10 chords, wavelength resolution of 0.02 nm per pixel, and looking at the C III line at 464.742 nm. Lastly, the instrument produces its own broadening of lines, which is a Gaussian of $\sigma = 0.06$ nm for a zero temperature line. Typically a thousand points along the chord is sufficient, with less than 0.1% difference from increasing this to ten thousand points.

The most basic profile would be to assume all of intensity, velocity, and temperature, are parabolic. The results of applying the three methods to a case with parabolic profiles is shown in figure 4.1. In figure 4.2, the results of fits to a second case are shown, where temperature and velocity have a parabolic profile, but the intensity profile drops to zero near the middle radius. This gives a hollow profile that would be seen, for example, if the particular species was not present at the hottest part of the plasma due to ionization. The lack of intensity at a point, and low intensity for a region, is difficult for fitting algorithms, as the observed spectra would be dominated by the effect of brighter regions.

The fitting methods provide comparable results when fitting the velocity profiles. The center of mass and stepped method slightly underestimate velocity. The center of mass method has limited resolution for temperature when the FWHM is found by counting the pixels above the half-max as plotted. Although this may be potentially improved by interpolating to find the FWHM with sub-pixel accuracy. Negative temperature corre-

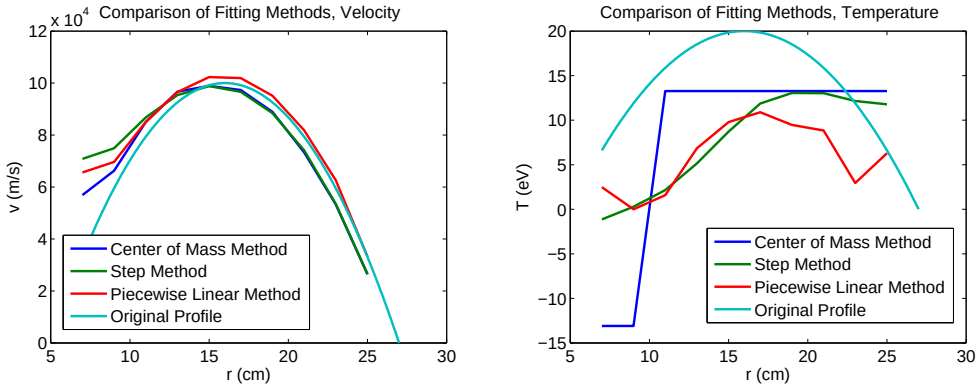

Figure 4.1: These plots compare fits of the discussed deconvolution methods given an ideal case with parabolic intensity, velocity, and temperature radial profiles.

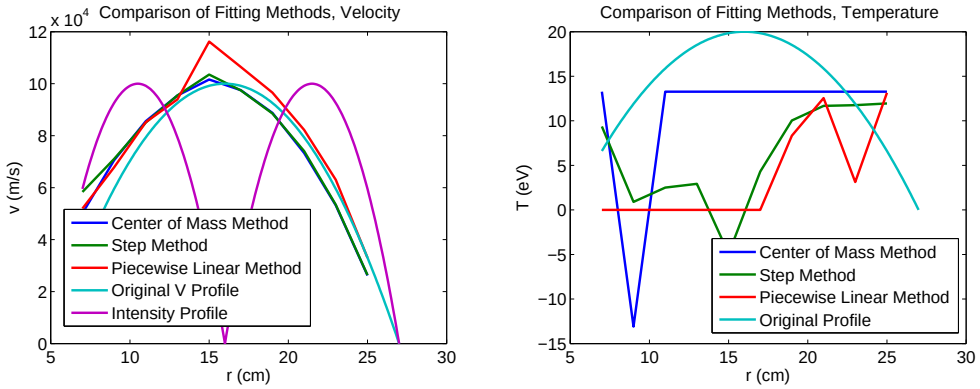

Figure 4.2: These plots compare fits of the discussed deconvolution methods given a parabolic velocity and temperature radial profiles, but an intensity profile that goes to zero in the middle (plotted in the velocity plot on left).

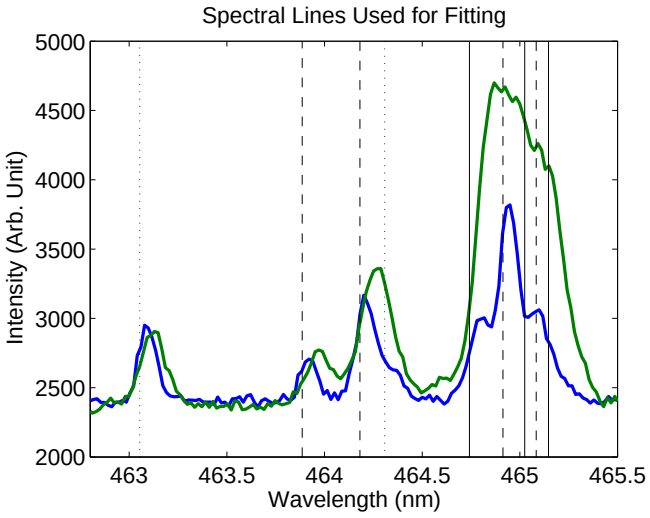

Figure 4.3: Two chords, outermost in blue and the fifth of ten in green, are shown for a mirror ratio 7 shot. The unshifted spectral line positions are show by vertical bars, with solid for C III, dashed for O II, and dotted for N II.

sponds to the case of a line width found to be smaller than that expected from instrumental broadening.

The previous test cases were for a single spectral line, a CIII line at 464.742 nm. This line actually overlaps with a few OII and CIII lines, and in the near vicinity are some OII and NII lines. While in previous years, the CIII line was quite a bit stronger than other overlapping lines, improvements to the vacuum system, especially removing an oil based roughing pump, have reduced the carbon content. Including the nitrogen and oxygen lines away from the main CIII line helps resolve velocity and temperature of oxygen, to allow removal of oxygen lines overlapping with the CIII lines. As these species are expected to rotate at slightly different speeds due to their differing q/m ratios, the center of mass method is not appropriate. The lines being considered are listed in table 4.1 and an example spetrum is plotted in figure 4.3. All of the lines fall within a window between 462.5 and 465.5 nm.

Species	λ_0 (nm)
NII	463.054
OII	463.88550
OII	464.18104
NII	464.308
CIII	464.742
OII	464.91348
CIII	465.025
OII	465.08394
CIII	465.147

Table 4.1: The lines listed above are the lines examined for Doppler broadening and shift in the 462.5 to 465.5 nm window.

4.4 Experimental Setup

There are two components to the experimental setup for the spectroscopy measurements: the collection half that collects light from the plasma into fiber optic cables, and the spectrometer half that records the spectra from light on the other end of the fibers.

The collection optics consist of a 1/2" optical tube with a fiber connection on one end and a plano-convex lens on the other end with 40 mm focal length. The location of the lens is adjustable to match the focal point with the entrance to the fiber. Focus is adjusted by back-illuminating the setup with a diode laser on the other end of the fiber, and adjusting to achieve a beam of consistent diameter on the order of a meter.

These lens assemblies are mounted on optical posts, which then mount to an optical breadboard mounted to the side of an MS coil, either viewing through a window at midplane, or at the transition region. To aim the lenses, the mounting location and desired impact parameters of the chords are used to calculate the intersection point with the vacuum window. By back-illuminating the lens assemblies, they are aimed to the correct position on the window. Additionally, this allows the ability to double check that the beams reach the main chamber as opposed to intersecting the vacuum vessel before reaching where the plasma will be.

The central piece of equipment on the recording end is a McPherson, one meter, Czerny-Turner spectrometer employing a 1200 line/mm reflective diffraction grating. The spectrometer was moved further away from the vacuum vessel in the next room over, in the hope of reducing vibrations from plasma discharges. The ten incoming fibers from the ten different chords are multiplexed by an adapter that couples each incoming fiber with multiple smaller fibers, then arranges these smaller fibers to reshape the output into ten, colinear rectangles. An adjustable input slit on the spectrometer is then used to

additionally collimate the output. A slit width of 50 microns was used, as a balance of enough, consistent light (slits were only parallel to within a few microns) with increased resolution due to narrower projected lines.

The output of the spectrometer went to a Stanford Optics 4-Quik E intensified CCD camera, with a horizontal resolution of 768 pixels. The camera has adjustable gain, controlled by a voltage of 0-1000 V applied to a multichannel plate within the camera. The gain has a nonlinear response to the applied voltage, although only a single gain is used for a given set of data and this does not impact the relative intensity needed for deconvolution. The camera has electronic shuttering/gating that allows for a single image to be taken during each shot, integrating light over the shutter time.

A plano-convex cylindrical lens with approximately 10 cm focal length was added between the camera and spectrometer output to fix a slight astigmatism in the spectrometer output. The lens was used to strengthen the focus in the vertical direction.

4.5 Calibration

Two components of the spectrometer need to be calibrated: the wavelength vs. horizontal pixel calibration and the relative intensity of different chords. All calibrations are done with the complete system, using the same collection optics as used on the plasma, and repeated for each chord.

The positioning system for the diffraction grating contains significant backlash, and is only good enough for returning the spectrometer to roughly the same position. Exact calibration is achieved by taking long integrations (or summing multiple images) of calibration lamps with known lines. For calibration when observing around the 465 nm CIII line, a neon lamp is used that produces both NeI and MoI lines (the latter likely due

to molybdenum being a common electrode material in discharge lamps). The lines from the calibration lamp can be used to estimate the instrument broadening, by assuming the lamp is at roughly zero temperature. Calibration from lines is done before and after every day of data taking to check for changes or issues, for example if calibration was changed due to bumping the spectrometer.

Initially calibration lines are associated with actual lines by an algorithm that cycles through every pair of peaks seen in a calibration image and every pair of lines from spectral database, derives a linear relation between pixel and wavelength, then counts how many other observed lines fall with a few pixel threshold of an actual line. To speed the process up, pairings are skipped if the pixel/wavelength ratio is outside of a generous range about the expected ratio (typically 0.017-0.019 nm/pixel around the 400-500 nm range). The pairing with the highest number of matches is then used as a starting point for a fitting algorithm that is essentially a least square residual fit to the sum of Gaussian functions, one for each matched peak, on top of a polynomial background. The final calibration fit can be higher order than linear; however higher order fits were found to change differences between observed and known line positions by 0.01 nm or less (less than half a pixel), with less than a 10% reduction in square residual. Therefore, linear calibrations will be used. Figure 4.4 shows an example of a calibration spectrum and matched lines.

The calibration varies by less than 0.02% or 0.005 nm when the process is repeated immediately to test for any variation in assembling the calibration setup. On the other hand, day to day variation in the calibration can be on the order of 0.1% or 0.02 nm, necessitating calibration every day. Calibration also varies up to 0.02 nm between chords, due to projection of chord spectra into the camera not being perfectly parallel with rows of pixels.

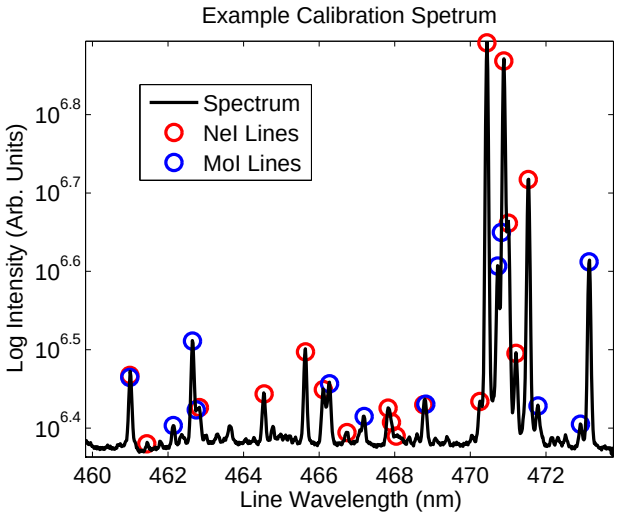

Figure 4.4: This plot shows an example spectrum from a neon discharge lamp showing both NeI and MoI lines.

The calibration spectral lines can also be used to give a rough estimate of relative intensity between chords, although this only works at the specific places where there are lines in the calibration source. Additional intensity calibration can be done by using a Labsphere brand halogen lamp and integrating spere as a white light source that provide a calibrated source of roughly blackbody light. Although the intensity calibration is performed with all optical components present to account for absorption in any particular component, this calibration done with the collection assembly on a mount away from the machine. Remounting the lens assembly could introduce variations in intensity due to change in stresses and bending of fibers that may lessen transmission.

Example measurements of relative intensity are plotted in figure 4.5. This includes measurements based both on the spectral lines in a neon lamp, and a white light source. The former has larger variations compared to a white light source calibrated for a specific output level. Using just the white light source, relative intensity can be calibrated to

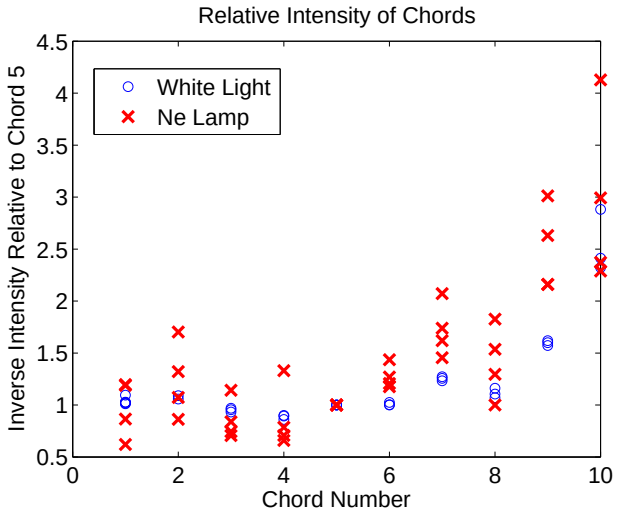

Figure 4.5: This plot shows measurements of relative intensity of the different chords relative to chord number 5. The plot displays this as the inverse of the relative intensity, i.e. the correction factor to multiply by to yield consistent intensity. So for example, chord 10 is relatively dim, and must be multiplied by a factor of 2-3 for equivalent intensity.

about 2% error except for the exceptionally dim chord 10. This chord is used for the inner most chord, where the loss of accuracy will have the least impact on other measurements after convolution.

4.6 Results

Velocity and temperature fits to spectroscopy data for mirror ratio 7.8 are shown in figure 4.6. A clear peaking of velocity toward the central radii is seen, with a peak C III velocity of 105 ± 5 km/s. Error bars in the plot are from standard deviation of shot-to-shot variation. The second innermost chord was dropped from the plots due to the deconvoluted intensities for this chord being zero, allowing velocity and temperature to be unconstrained. This likely was a result of intensity calibrations disagreeing with actual relative intensity for that chord.

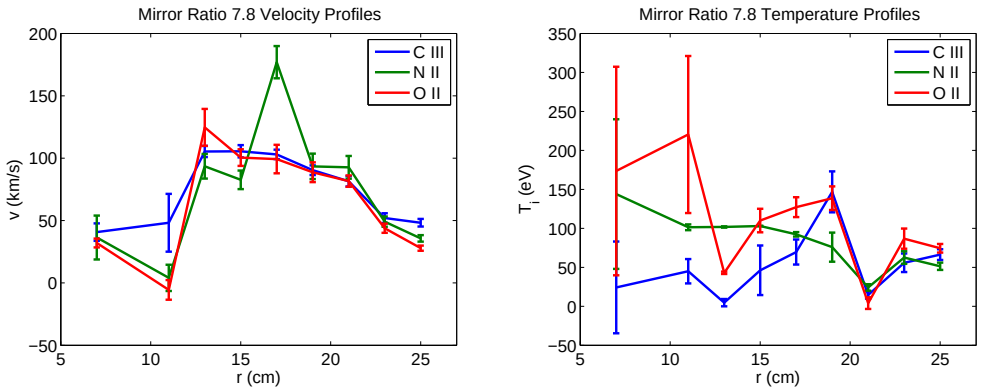

Figure 4.6: These plots show velocity and temperature profiles from spectroscopic data for mirror ratio 7.8. Error bars are standard deviation of shot-to-shot variations.

Temperature shows a possible similar peaking, with large error bars on innermost chords due to the deconvolution process. Looking at the 4th to 6th chord suggests a temperature for C III in the middle of the plasma of 87 ± 25 eV.

Similar results for mirror ratio 3.2 are shown in figure 4.7. This data was fit to spectroscopy data from a $z = 75$ cm in the transition region, due to low light intensity at the midplane. The outermost three chords also had low intensity and rough fits, while the deconvolution process fit inner chords much better. The velocity peak toward the middle radius for C III is 87 ± 5 km/s. Temperature fits from the mirror ratio 3 shots were not salvagable.

4.7 Comparison with Older Spectroscopy

The temperatures and velocities measured above are higher than values previously reported [6], as an increasing trend has been seen [26]. In figure 4.8, an example N II line shown both from late 2010 (when earlier spectroscopy data was taken) and from early 2010. The newer one is from the 5th chord out of the ten chord setup, while the older

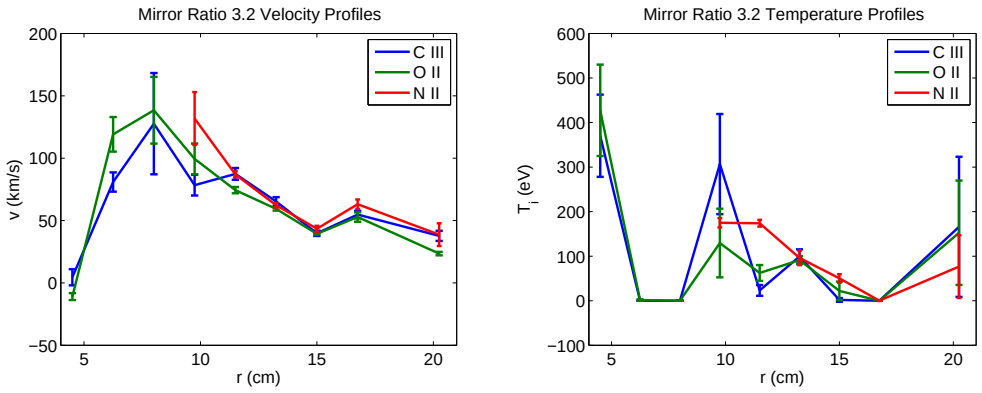

Figure 4.7: These plots show velocity and temperature profiles from spectroscopic data for mirror ratio 3.2. Error bars are standard deviation of shot-to-shot variations.

shows the third chord from an older five chord setup.

The newer spectra shows a slightly faster velocity, with the peak corresponding to 40 km/s as opposed to the older 33 km/s. The velocity of the raw, chord spectrum is not the peak velocity, but a crude lower bound due to the chord receiving light from lower velocity outer layers. This increase in velocity is also seen partially in a 10% increase in voltage across the plasma which correlates with rotation velocity. [23]

The temperature is larger in the newer data, with a Gaussian fit to the raw chord spectrum giving 230 eV for the newer spectrum versus 110 eV for the older spectrum. As with the velocity representing a lower bound, these temperature values are an over estimate of temperature, especially due to supersonic velocities between layers.

This increase in temperature and velocity has been speculated to be from cleaning and removal of impurities from the vacuum system, as briefly discussed in Section 2.4. As the increase occured with roughly the same time as incremental vacuum improvement, intensity of impurity lines were also seen to decrease as a result of the cleaning.

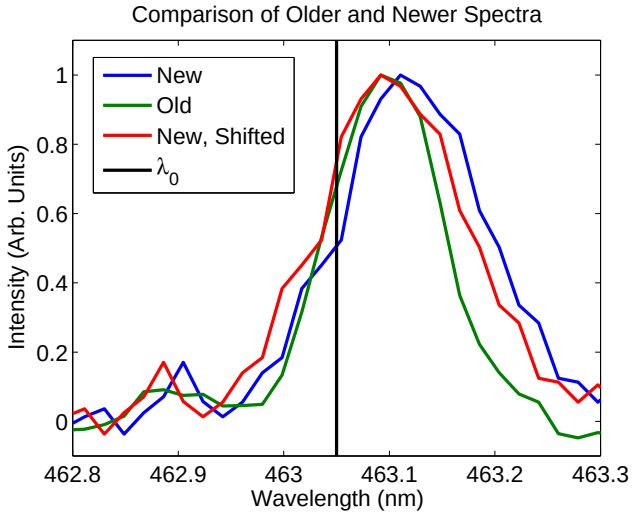

Figure 4.8: This plot shows changes in the 430.05 nm NII line over from early to late 2010. The newer spectra is plotted twice, with the red curve shifted to the same peak as the older spectra to show different in temperature.

Chapter 5

Diamagnetic and Pickup Loops

This chapter concerns two different systems of magnetic loops on the MCX experiment external to the vacuum vessel: Diamagnetic loops (DMLs) which measure flux in the $r - \phi$ plane over the whole such cross-section of the machine, and B_r pick-up loops which measure the radial flux through a much smaller cross-section.

5.1 Principles of Operation

Magnetic fields created by the plasma are measured by simple loops and coils of wire to measure the voltage created by a change in flux:

$$V = NA\frac{dB}{dt}$$

The resulting voltage reflects only the change in magnetic flux, which has the added advantage of disregarding the unchanging background vacuum magnetic field. Since fields of interest are on the order of 1-100 G on a background field of 2-14 kG, this avoids sensitivity and saturation issues seen by DC sensitive measuring methods like Hall effect probes.

Integration is required to retrieve the original magnetic field information from the voltage, which may be done either electronically on the signal before recording by data acquisition, or numerically after the signal was acquired. The former can allow for filtering out of higher frequencies and noises that could lead to aliasing issues when recording, but also complicates the frequency response and calibration of the probes. The latter method has been chosen instead.

Without the electronic integrator such that the circuit consist of just the loop and a high impedance data recording system, the cutoff frequency of the loop itself is quite high leaving the frequency response to be determined by the shielding effects of any metal between the loop and the field to be measured. In the case of probes measuring the field inside the vacuum vessel, this shielding would come from a thin conducting electrostatic shielding around the loop. In the case of the DMLs and B_r coils, the shielding comes from the stainless steel vacuum vessel.

5.2 Effects of Vacuum Vessel

The effects of the vacuum vessel can be approximated by solving Maxwell's equations for an infinitely long hollow cylinder of conductivity σ, with a magnetic field of the form $\mathbf{B} = \hat{B}(r)e^{-i\omega t}\mathbf{z}$. From Ampere's law, disregarding Maxwell's correction as wavelength being considered is small compared to the size of the system, along with Ohm's law and Faraday's law, all for the region within the conducting cylinder:

$$\begin{aligned}
\nabla \times \mathbf{B} &= \mu\mathbf{J} \\
\nabla \times \mathbf{B} &= \mu\sigma\mathbf{E} \\
\nabla \times (\nabla \times \mathbf{B}) &= \mu\sigma\nabla \times \mathbf{E} \\
\nabla \times (\nabla \times \mathbf{B}) &= -\mu\sigma\frac{\partial \mathbf{B}}{\partial t} \\
\nabla \times (\nabla \times \mathbf{B}) &= \mu\sigma\omega i\mathbf{B}
\end{aligned}$$

Dropping derivatives with respect to z and ϕ gives for the left hand side:

$$\begin{aligned} \nabla \times \left(-\frac{\partial B_z}{\partial r}\hat{\phi} + \frac{1}{r}\frac{\partial}{\partial r} r B_\phi \mathbf{z} \right) &= \mu\sigma\omega i \mathbf{B} \qquad (5.1) \\ -\frac{\partial}{\partial r}\frac{1}{r}\frac{\partial}{\partial r} r B_\phi \hat{\phi} - \frac{1}{r}\frac{\partial}{\partial r} r \frac{\partial B_z}{\partial r}\mathbf{z} &= \mu\sigma\omega i \mathbf{B} \\ -\frac{1}{r}\frac{\partial}{\partial r} r \frac{\partial \hat{B}}{\partial r} &= \mu\sigma\omega i \hat{B} \\ r^2 \frac{\partial^2}{\partial r^2}\hat{B} + r\frac{\partial}{\partial r}\hat{B} + i\mu\sigma\omega r^2 \hat{B} &= 0 \qquad (5.2) \end{aligned}$$

Defining $K = \mu\sigma\omega = 2/\delta^2$ (δ is the skin depth), the above is the Bessel differential equation which would give a solution for $\hat{B}$ in terms of the two Bessel functions as:

$$\hat{B} = c_1 J_0(\sqrt{iK}r) + c_2 Y_0(\sqrt{iK}r)$$

Instead of solving boundary conditions with the general Bessel solution, the thinness of the vacuum vessel can be used to reduce equation 5.2 with the substitution $r \to r_0 + x$ with $x \ll r_0$:

$$\frac{\partial^2}{\partial x^2}\hat{B} + \frac{1}{r_0}\frac{\partial}{\partial x}\hat{B} + i\mu\sigma\omega\hat{B} = 0$$

If the skin depth is much smaller than the inner radius r_0 of the vessel, then the second drops off giving:

$$\frac{\partial^2}{\partial x^2} B + i\mu\sigma\omega\hat{B} = 0 \qquad (5.3)$$

The solution reduces down to an exponential:

$$\hat{B} = c_1 e^{\sqrt{iK}x} + c_2 e^{-\sqrt{iK}x} \qquad (5.4)$$

Let Δ be the vessel wall thickness, then the requirement that the magnetic field outside of the vessel be zero gives:

$$\begin{aligned} \hat{B}(r_0 + \Delta) &= 0 \\ c_1 e^{\sqrt{iK}\Delta} + c_2 e^{-\sqrt{iK}\Delta} &= 0 \\ c_2 &= -c_1 e^{2\sqrt{iK}\Delta} \qquad (5.5) \end{aligned}$$

Now given some flux Φ within the vessel varying at ω, with $B_0 = B(r_0) = c_1 + c_2$, Ohm's law and Ampere's law gives for the inner surface of the vessel:

$$\begin{aligned}
j_\phi &= \sigma E_\phi \\
\frac{1}{\mu}\frac{\partial}{\partial r}\hat{B}\Big|_{r=r_0} &= \frac{-i\sigma\omega}{2\pi r_0}(\Phi - \pi r_0^2 B_0) \\
c_1 - c_2 &= -\frac{i\sigma\omega\mu}{2\pi r_0\sqrt{iK}}(\Phi - \pi r_0^2 B_0) \\
c_1(1 + e^{2\sqrt{iK}\Delta}) &= -\frac{\sqrt{iK}}{2\pi r_0}(\Phi - \pi r_0^2 B_0) \\
B_0\frac{1 + e^{2\sqrt{iK}\Delta}}{1 - e^{2\sqrt{iK}\Delta}} &= -\frac{\sqrt{iK}}{2\pi r_0}(\Phi - \pi r_0^2 B_0) \\
\pi r_0^2 B_0\left(\frac{\coth\Delta\sqrt{iK}}{\pi r_0^2} + \frac{\sqrt{iK}}{2\pi r_0}\right) &= \frac{\sqrt{iK}}{2\pi r_0}\Phi \\
\frac{\pi r_0^2 B_0}{\Phi} &= \frac{1}{\frac{2\coth\Delta\sqrt{iK}}{r_0\sqrt{iK}} + 1}
\end{aligned} \tag{5.6}$$

Assuming the vessel wall is thin again such that the flux within the vessel wall is negligible, the left hand side of 5.6 gives what proportion of the flux Φ is being shielding by the flux created by the vessel's response. Putting in the values appropriate for a 1/8" thick stainless steel vessel, this gives a 3 dB cutoff frequency for the 27.6 cm, 22.5 cm, and 18.7 cm sections as 125 Hz, 153 Hz, and 184 Hz, which correspond to L/R times of 1.3 ms, 1.1 ms, and 0.8 ms.

5.3 Construction and Calibration

The construction of the DMLs is quite simple when done outside of the vacuum, and consists of turns of wire wrapped around the vacuum vessel. All DMLs were constructed with three turns of wire. The DMLs at $z = \pm 65$ and ± 102 cm were taped down to prevent movement. The DMLs located from $z = 8$ to 48 cm were more difficult to install due to the small gap between the vacuum vessel and the solenoid magnet coil casing. These had to be wound at the end of the machine, then slid along the vacuum vessel to the appropriate

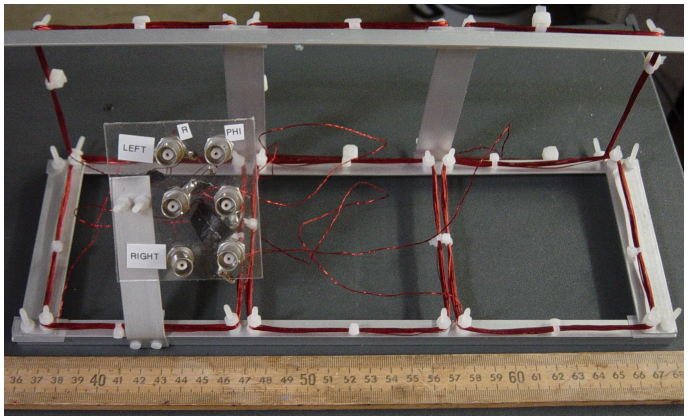

Figure 5.1: This is a photo of the loop array used for measure B_r in the z range from 65 to 95 cm. The extra set of loops visible at the top of the photo were intended to measure B_ϕ external to the vacuum vessel, but are not discussed here.

z, which was not directly visible for $z = 16$ and 32 cm. This leads to a larger error in positioning of the coils, on the order of ± 0.5 cm, including the possibility of a tilt relative to the z-ϕ plane. DMLs are typically connected directly to the MCX DAQ system, or fed through an attenuator when necessary to limit signal to the DAQ voltage limits of ± 10 volts.

The B_r pickup loops were made in two designs: one for the axial arrays, and one for the azimuthal arrays. The axial arrays consisted of a parallel pair of aluminum 3/8" angle bars, so as to easily sit on the round vacuum vessel, with protruding nylon screws to support the pick-up coils, as shown in figure 5.1. These had 25 turns of enamel coated 28 gauge wire, with an area of 4"x3.625". The bulk of the wire and flexibility of the nylon screws limits the position of the individual loops of the coil to about ± 0.2 cm. There were three axial arrays made, one with five loops meant for the $z = 10$ to 65 cm range, and two made to fit between the flanges and jogs in the $z = 65$ to 95 range.

The azimuthal B_r array consists of 16 pick-up coils each of 25 turns of the same

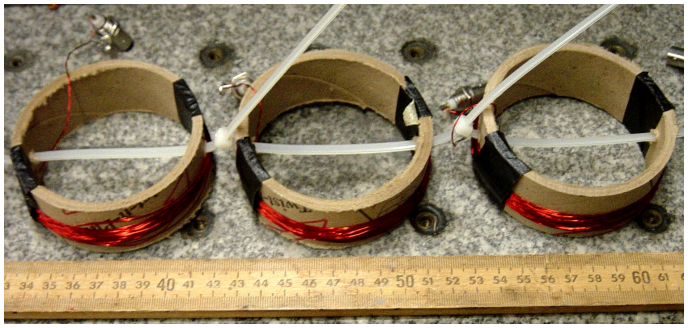

Figure 5.2: This is a photo of the loop array used for measure B_r for axial positions with z below 65 cm. Only three loops are visible in the image, with the complete belt containing 16 evenly spaced loops. Loops were attached to the vessel by tensioning the plastic wire ties between them, with each loops position adjusted individually to achieve even spacing at the same axial position.

wire as the other B_r arrays. These were wound around cardboard tubes with an outer diameter of 3.25" as shown in figure 5.2. The individual loops would range from 0.5 to 2.0 cm above the vacuum vessel, as the solenoid coil had a length of about 1.5 cm. This array was designed to be moved in the z direction between shots, so the position of each individual loop was subject to varying error in both z and ϕ position (the loops were not rigidly connected to each other). Similar to the DMLs in the same range, when positioned between the vessel and the solenoid magnet casing, positioning errors were likely higher due to limited visibility.

Both DMLs and B_r loops could be calibrated in situ by recording their response to the creation of the vacuum magnetic field. There are several ways to interpret calibration of the loops. The simplest is to compare the measurement and expected field to get a factor C that expresses how much flux there is per integrated voltage signal:

$$\Phi = C \int V(t) dt$$

This factor depends on the area, angle, and number of turns of the loop, so calibration

in this way assumes the area is not know that well due to variations in the construction. Alternatively, if the size of the loop is well constrained, the calibration can instead attempt to fit the location of the loop within the field. For example, the radius of the DMLs are well constrained by the vacuum vessel as a single layer coil (as opposed to a coil with turns wrapped on top of other turns), but their position in z has larger uncertainties where the loops are not in a visible location.

5.4 Azimuthal Asymmetry

The B_r belt allows for testing of slow timescale azimuthal symmetry of the B_r field. B_r measured at several different z locations, for mirror ratio 7.8 and 3.2, are shown in figure 5.3. Variations of 5-10 gauss were found. This variation is about 15-30% of the largest B_r measurements, although can be larger than the symmetric component of the B_r in some places as B_r can pass through zero. The structure of the variations depends on the mirror ratio, with a with a m=2 structure were observed, with weaker variations for lower mirror ratios. If the mean across azimuth are subtracted, these variations are seen to be constant across $|z| < 65$ cm, as shown in contour plots in figure 5.4. The angle labeled zero corresponds to top of the vessel, with increasing angle going clockwise as viewed from the high voltage end of the machine.

These variations are locked modes, in the sense they do not rotate with the plasma and have a fixed azimuthal position across shots. As seen in figure 5.5, the modes change little with time, especially for higher mirror ratios.

As a test of the source of these asymmetries, an insulating large obstacle (a 1 inch diameter by 2 inch long boron nitride cylinder on the end of an insulating rod) was inserted into the plasma at midplane, as shown in figure 5.6. Insertion past a certain

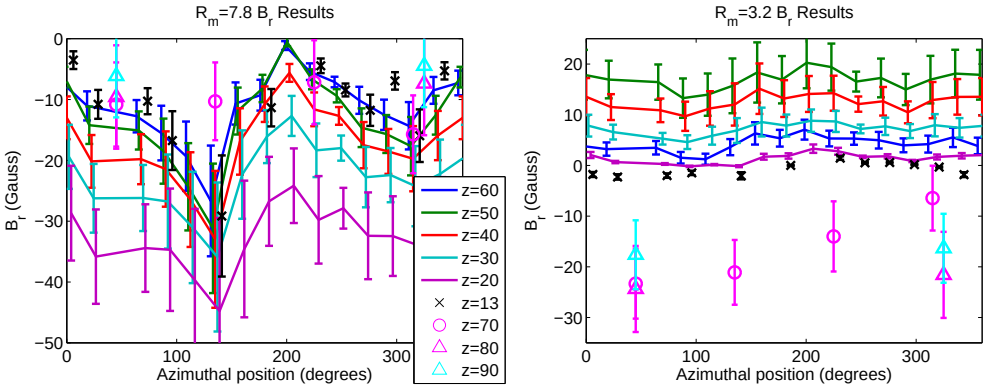

Figure 5.3: Plots of different azimuthal dependence of B_r for different z positions for mirror ratio 7.8 and 3.2. For $z > 65$ cm, B_r is only measured with discrete loops at fewer azimuthal positions. Also, at innermost $z = 13$ cm, some loops were damaged by positioning of loops, and are not plotted.

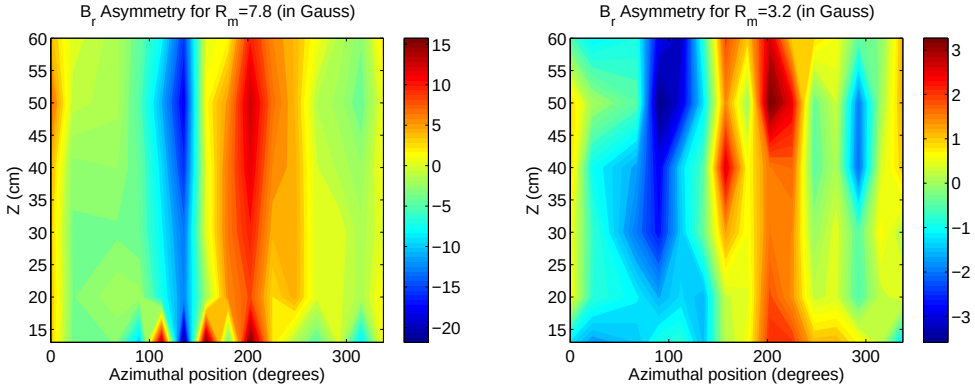

Figure 5.4: Contour plots of different azimuthal dependence of B_r for different z positions for mirror ratio 7.8 and 3.2. The average value over azimuthal angle is subtracted for each z to display only the asymmetric component of the field. Only size z location measurements are used here with linear interpolation between them. Large positive spikes at $z < 15$ cm at middle angles are due to three damaged loops. Each curve is an average of 5-10 shots.

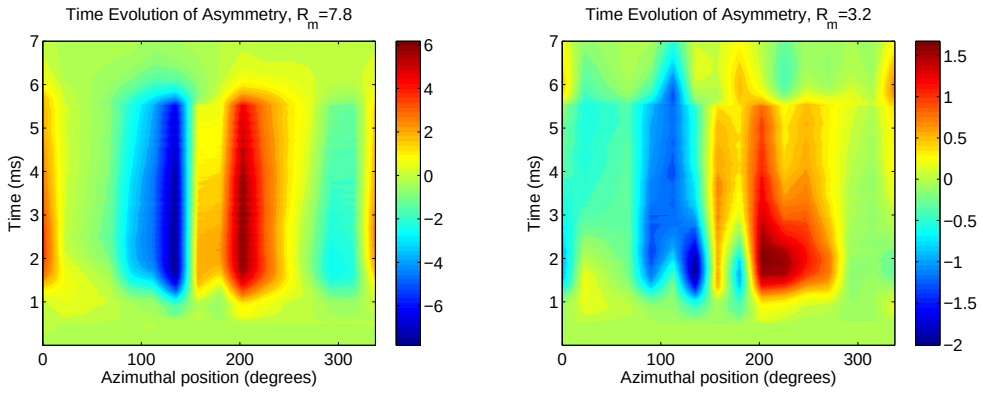

Figure 5.5: These contour plots show the time evolution of the azimuthal B_r asymetry for (with azimuthal mean for each time subtracted) mirror ratios 7.8 and 3.2. These are for measurements at $z = 60cm$. Each is an average of 5-10 shots.

radius produced a change in structure, reducing m=2 component of the asymmetry. This suggests the asymmetries come from asymmetries in how the plasma is limited by the vacuum vessel. One possibility is an azimuthal array of internal magnetic loops near the jog in vacuum vessel that limits the plasma for mirror ratios below 8. Asymmetries at midplane from vacuum ports and a metal shield that projects about a centimeter inside the vacuum vessel that covers some cabling may affet higher mirror ratios. Additionally reversal of the direction of the vacuum field did not have major effects on te asymmetry.

In later sections, these asymmetries will be removed by averaging over azimuthal angle to give a B_r value for each measured z. However this necessitates measurements with the B_r belt as opposed to an array of loops at a single azimuthal position.

5.5 Results

This section discusses some basic results and measurements of the DMLs and B_r loops. More detailed results appear in a later chapter comparing the measurements to

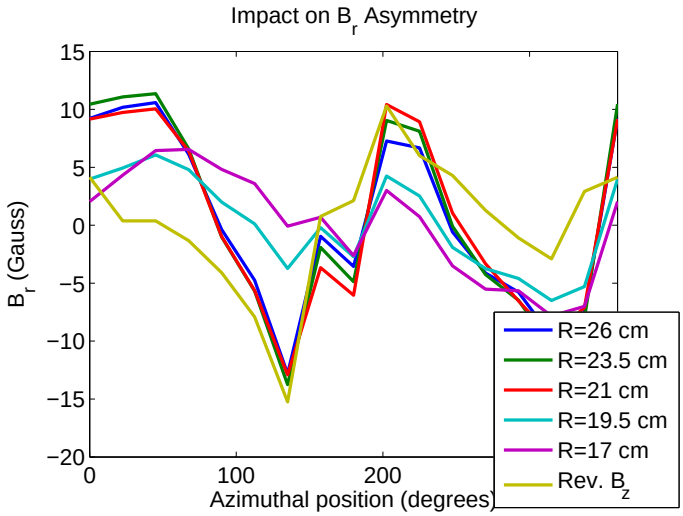

Figure 5.6: The first five curves show the effect of inserting a large, non-conducting obstacle into the plasma at midplane. The last curve shows the effect of reversing the vacuum B_z field direction.

theory.

There are a few ways DML measurements can be presented: as a flux, as an average B_z across the DML area, and as an average B_z across the plasma cross section. The last requires assuming the position of the LGFS and that the plasma is mostly confined within those flux surfaces. While this is simple using the vacuum field, bowing out of field lines from plasma pressure changes this area. Instead the average B_z across their entire area will be used, taking into account the different area of loops on difference radii sections of the vacuum vessel, except for an example plot in figure 5.8 showing an average of the vacuum field LGFS.

The raw, unintegrated DML signals and calibrated integrated signal of an example mirror ratio 7.8 shot are shown in figure 5.7. The DML results for mirror ratio 7.8 and 3.2 are shown in figure 5.8 after averaging over a time window. The higher mirror ratio shows a large amount of expelled flux near the midplane, while the lowering mirror ratio

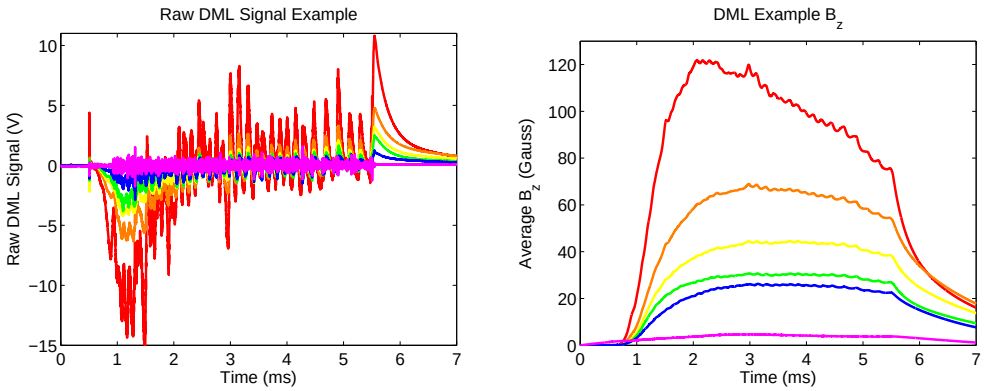

Figure 5.7: These plots show time evolution of raw and integrated DML signals. Calibration factors are applied to the integrated signal, and the raw signal had attenuator effect removed. Colors follow the rainbow from red for innnermost DML at $z = 8$ cm to outermost DML at $z = 104$ cm in magenta.

shows two off-midplane peak in expelled flux near the $z = 66$ cm DML. This is consistent with expecting the plasma to be around the minima of the vacuum field, as lower mirror ratio vacuum fields have an additional pair of field minima off-midplane. Of particular note, the symmetry in DML measurements across the midplane is within 5%, or within 1% when looking at DMLs at $z = \pm 8$ cm.

The results are averaged from averaging over a 1 ms window starting at 3.5 ms after breakdown. A comparison of averaging over different time windows is shown in figure 5.9.

Results from the B_r belt and other B_r loops are displayed in figure 5.10, where values are averaged over azimuthal angle for a given axial position. These results are consistent with B_z measurements, where for mirror ratio 7.8 field lines can be seen to point inward with increasing z corresponding to the field lines bowed out at midplane. Likewise, for mirror ratio 3.2, the B_r corresponds to field lines bowing outward at the off-midplane vacuum field minima.

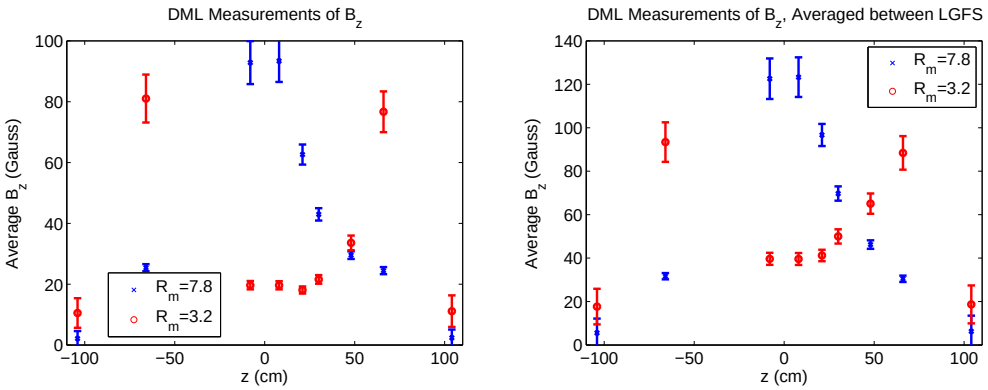

Figure 5.8: These plots show DML measurements averaged over a time of 3.5-4.5 ms after breakdown. The plot on the left shows B_z averaged over entire cross-section area of DMLs, while on the right is shown averaged over the cross-section area of LGFS as determined from the vacuum field.

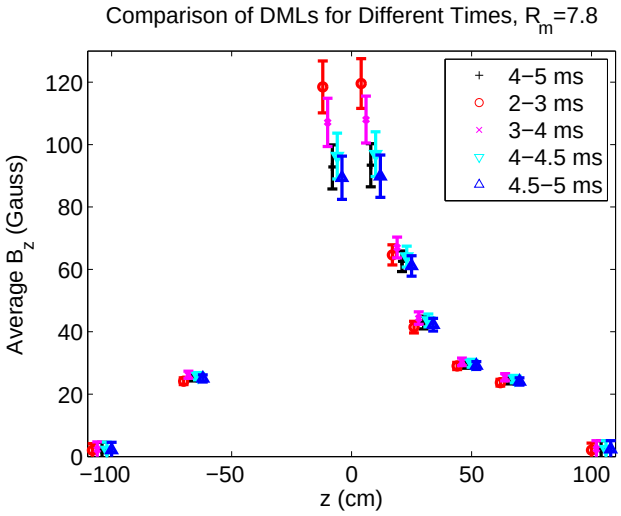

Figure 5.9: This plot shows a comparison of averaging DML signal over different time windows. Points are shifted in z for clarity of error bars.

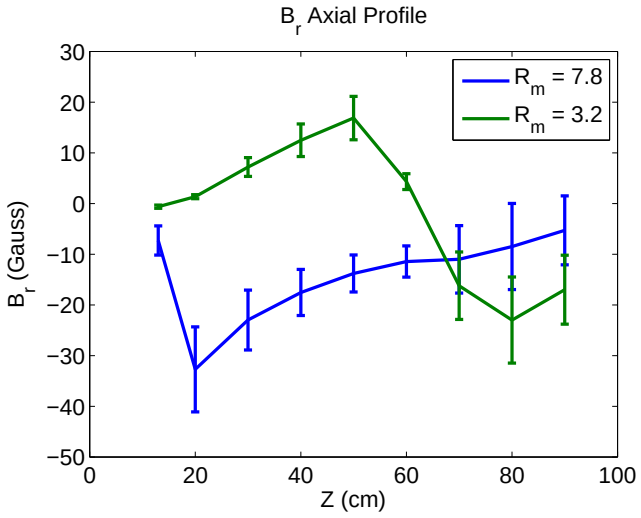

Figure 5.10: This plot shows a comparison of averaging DML signal over different time windows. Points are shifted in z for clarity of error bars.

5.6 Discussion of Errors

The errors for the magnetic measurements have two components: errors in calibration, including positioning of loops, and shot-to-shot variation. For DML measurements, the error in loop calibration is comparable to about 50% larger than the errors from variation between shots. While for B_r loops, calibration errors are expected to be a factor of 5-10 larger than shot variations.

For DML loops, the errors in calibration can come from error in cross-section area, error in angle of loop with respect to z axis, and error in axial position. Errors in radii of loops are on the order of millimeters or less, which gives at most a 2% error in cross-section area. Errors in positioning of the loop can vary from a few millimeters for the visible loops at $z \geq 66$ cm, while up to a centimeter for loops not visible under magnet coils. Even with a tilt due to a centimeter difference in z position of opposite sides of DML coils, this gives a less than 2% error in flux through the loop. A centimeter error in axial position

can introduce another 2% error in calibration factor.

The B_r loops experience similar sources of errors due to positioning. However, because the B_z field is larger than the B_r component, errors in angles of loops can introduce a larger error from picking up a portion of the B_z component. The error estimates from area, angle, and positioning are estimated to be 3%, 10-20%, and 5% respectively. Additional errors may also be introduced from averaging over azimuth depending on positioning loops relative to the azimuthal locked modes and assuming an average of the loops represents an average over the azimuthal angle. This results in larger error for $z > 65$ cm from only 4 or 2 loops used per axial position compared to the 16 loops in the belt, due to vacuum vessel ports preventing placement of additional loops.

Chapter 6

MHD Theory

This chapter discusses how ideal MHD theory can be applied to the MCX geometry and diamagnetism, and provides a framework for comparison between theory and data.

6.1 Grad-Shafranov Equation

The goal of these derivations is to express the effects of rotation and plasma pressure on the magnetic field lines. An axial, axisymmetric magnetic field can be expressed as:

$$\mathbf{B} = \nabla\phi \times \nabla\psi \tag{6.1}$$

where $\nabla\phi = \hat{\phi}/r$ and define:

$$\nabla\Phi = \mathbf{u} \times \mathbf{B} \tag{6.2}$$

Since $\mathbf{B} \cdot \nabla\Phi = 0$, this implies Φ is a function of ψ, (i.e. $\Phi = \Phi(\psi)$).

$$\begin{aligned}
\nabla\Phi &= \mathbf{u} \times (\nabla\phi \times \nabla\psi) \\
\nabla\Phi &= (\mathbf{u} \cdot \nabla\psi)\nabla\phi - (\mathbf{u} \cdot \nabla\phi)\nabla\psi \\
\Phi'(\psi)\nabla\psi &= -(\mathbf{u} \cdot \nabla\phi)\nabla\psi \\
\Phi'(\psi) &= -(\mathbf{u} \cdot \nabla\phi)
\end{aligned}$$

Assuming the motion is rotational, $\mathbf{u} = u_\phi\hat{\phi}$, then this gives

$$u_\phi = -r\Phi' \tag{6.3}$$

From the MHD force balance, then dotting $\mathbf{B}$ into both sides:

$$\begin{aligned}
\rho\mathbf{u}\cdot\nabla\mathbf{u} &= -\nabla p + \mathbf{j}\times\mathbf{B} \\
\rho\frac{u_\phi}{r}\frac{\partial}{\partial\phi}(u_\phi\hat{\phi}) &= -\nabla p + \mathbf{j}\times\mathbf{B} \\
-\rho\frac{u_\phi^2}{r}\hat{r} &= -\nabla p + \mathbf{j}\times\mathbf{B} \\
\rho\frac{u_\phi^2}{r}\mathbf{B}\cdot\hat{r} &= \mathbf{B}\cdot\nabla p \\
\rho r\Phi'^2\mathbf{B}\cdot\hat{r} &= \mathbf{B}\cdot\nabla p \\
\rho\left(r\Phi'^2\mathbf{B}\cdot\hat{r} + r^2\Phi'\frac{\partial}{\partial\psi}\mathbf{B}\cdot\nabla\Phi\right) &= \mathbf{B}\cdot\nabla p \\
\rho r\Phi'\mathbf{B}\cdot\nabla(r\Phi') &= \mathbf{B}\cdot\nabla p \\
\rho\mathbf{B}\cdot\nabla\frac{(r\Phi')^2}{2} &= \mathbf{B}\cdot\nabla p
\end{aligned}$$

Making the assumption that temperature is a function only of ψ, so that $T = T(\psi) = mc_s^2(\psi)$:

$$\begin{aligned}
\mathbf{B}\cdot\nabla p &= c_s^2(\psi)\mathbf{B}\cdot\nabla\rho + 2c_s(\psi)c_s'(\psi)\rho\mathbf{B}\cdot\nabla\psi \\
&= c_s^2(\psi)\mathbf{B}\cdot\nabla\rho \\
\frac{\mathbf{B}\cdot\nabla\rho}{\rho} &= \mathbf{B}\cdot\nabla\left(\frac{r^2\Phi'^2}{2c_s^2}\right) \\
\rho &= \rho_0(\psi)\exp\left(\frac{r^2\Phi'^2}{2c_s^2}\right) \qquad (6.4)
\end{aligned}$$

Equation 6.4 thus yields an expression for density, ρ, along a given field line ψ as a function of radius. Centrifugal confinement is seen by the exponential increase in density with radius.

Now dotting $\nabla\psi$ into the force balance equation:

$$\begin{aligned}
\rho\frac{u_\phi^2}{r}\hat{r}\cdot\nabla\psi &= \nabla\psi\cdot\nabla p - \nabla\psi\cdot(\mathbf{j}\times\mathbf{B}) \\
\nabla\psi\cdot(\mathbf{j}\times\mathbf{B}) &= \mathbf{j}\cdot[(\nabla\phi\times\nabla\psi)\times\nabla\psi] \\
&= (\mathbf{j}\cdot\nabla\psi)(\nabla\phi\cdot\nabla\psi) - \mathbf{j}\cdot\nabla\phi|\nabla\psi|^2 \\
&= (\nabla\psi\cdot[\nabla\times\mathbf{B}])(\nabla\phi\cdot\nabla\psi) - \mathbf{j}\cdot\nabla\phi|\nabla\psi|^2 \\
&= (\nabla\cdot[\nabla\psi\times(\nabla\phi\times\nabla\psi)] + \mathbf{B}\cdot[\nabla\times\nabla\psi])(\nabla\phi\cdot\nabla\psi) - \mathbf{j}\cdot\nabla\phi|\nabla\psi|^2 \\
&= -\mathbf{j}\cdot\nabla\phi|\nabla\psi|^2 \\
&= -(\nabla\times[\nabla\phi\times\nabla\psi])\cdot\nabla\phi|\nabla\psi|^2 \\
&= -[(\nabla\times[\nabla\phi\times\nabla\psi])\cdot\nabla\phi - (\nabla\pi\times\nabla\psi)\cdot(\nabla\times\nabla\phi)]|\nabla\psi|^2 \\
&= -\nabla\cdot[(\nabla\phi\times\nabla\psi)\times\nabla\phi]|\nabla\psi|^2 \\
&= -\nabla\cdot(|\nabla\phi|^2\nabla\psi)|\nabla\psi|^2 \\
&= -\nabla\cdot\left(\frac{1}{r^2}\nabla\psi\right)|\nabla\psi|^2
\end{aligned}$$

p and r can be expressed as functions of flux line and position along length of flux line, $p = p(\psi, l)$ and $r = r(\psi, l)$, then:

$$\begin{aligned}
\rho\frac{u_\phi^2}{r}\hat{r}\cdot\nabla\psi &= \nabla\psi\cdot\nabla p - \nabla\psi\cdot(\mathbf{j}\times\mathbf{B}) \\
\rho\frac{u_\phi^2}{r}\nabla r\cdot\nabla\psi &= \nabla\psi\cdot\nabla p - \nabla\psi\cdot(\mathbf{j}\times\mathbf{B}) \\
\rho\frac{u_\phi^2}{r}|\nabla\psi|^2\frac{\partial r}{\partial\psi} &= |\nabla\psi|^2\frac{\partial p}{\partial\psi} + \nabla\cdot\left(\frac{1}{r^2}\nabla\psi\right)|\nabla\psi|^2 \\
\nabla\cdot\left(\frac{1}{r^2}\nabla\psi\right) &= -\frac{\partial p}{\partial\psi} + \frac{\rho\Phi'^2}{2}\frac{\partial r^2}{\partial\psi} \qquad (6.5)
\end{aligned}$$

Equations 6.5 is the Grad-Shafranov equation accounting for supersonic rotation. Together with the density as given by 6.4, this expresses the diamagnetism in terms of profiles of temperature, rotation velocity, and the flux function component of density ρ_0.

6.2 Perturbative Solution

To reduce the Grad-Shafranov equation, the magnetic field produced by the plasma, $\tilde{\psi}$, can be treated as a perturbation on the vacuum field, ψ_0. For the vacuum field:

$$\nabla \cdot \left(\frac{1}{r^2} \nabla \psi_0 \right) = 0 \tag{6.6}$$

Then for the Grad-Sharfranov equation, using $p = c_s^2 \rho$, with ρ from equation (6.4), and $p_0 = c_s^2 \rho_0$:

$$\begin{aligned}
|\nabla\psi_0|^2 \nabla \cdot \left(\frac{1}{r^2} \nabla \tilde{\psi} \right) &= \frac{1}{2} \rho \Phi'^2 \nabla\psi_0 \cdot \nabla r^2 - \nabla\psi_0 \cdot \nabla p \\
&= \frac{1}{2} \rho \Phi'^2 \nabla\psi_0 \cdot \nabla r^2 - \nabla\phi \cdot \left[\nabla p_0 + \rho_0 \nabla \left(\frac{r^2 \Phi'^2}{2c_s^2} \right) \right] \exp\left(\frac{r^2 \Phi'^2}{2c_s^2} \right) \\
&= \nabla\phi \cdot \left(-\nabla p_0 + p_0 \left(\frac{\Phi'^2}{2c_s^2} \nabla r^2 - \nabla \left(\frac{r^2 \Phi'^2}{2c_s^2} \right) \right] \right) \exp\left(\frac{r^2 \Phi'^2}{2c_s^2} \right) \\
&= -\nabla\phi \cdot \left[\nabla p_0 + p_0 r^2 \nabla \left(\frac{\Phi'^2}{2c_s^2} \right) \right] \exp\left(\frac{r^2 \Phi'^2}{2c_s^2} \right) \\
\nabla \cdot \left(\frac{1}{r^2} \nabla \tilde{\psi} \right) &= -\left[\frac{\partial p_0}{\partial \psi_0} + p_0 r^2 \frac{\partial}{\partial \psi_0} \left(\frac{\Phi'^2}{2c_s^2} \right) \right] \exp\left(\frac{r^2 \Phi'^2}{2c_s^2} \right)
\end{aligned} \tag{6.7}$$

The three functions of flux in this equation, p_0, $\Omega = \Phi'$, and c_s^2, are now written in terms of an overall size times a form factor: $\rho_0 = \rho_{0,max} \hat{\rho}_0(\psi)$, $\Omega = \Omega_{max} \hat{\Omega}(\psi)$, and $c_s^2 = c_{s,max}^2 \hat{c}_s(\psi)$, where the max subscript indicates the peak value and a hat means a function between zero and one over ψ. Equation 6.7 then becomes:

$$\nabla \cdot \left(\frac{1}{\hat{r}^2} \nabla \hat{\tilde{\psi}} \right) = -\frac{M_A^2}{M_s^2} \left[\frac{\partial \hat{p}_0}{\partial \hat{\psi}_0} + M_s^2 \hat{p}_0 \hat{r}^2 \frac{\partial}{\partial \hat{\psi}_0} \left(\frac{\hat{\Omega}^2}{2\hat{c}_s^2} \right) \right] \exp\left(M_s^2 \frac{\hat{r}^2 \hat{\Omega}^2}{2\hat{c}_s^2} \right) \tag{6.8}$$

Here M_s and M_A have been defined as:

$$M_s = \frac{r_{mid} \Omega_{max}}{c_{s,max}} \tag{6.9}$$

$$M_A = \frac{r_{mid}^3 \Omega_{max} \sqrt{\rho_{max}}}{\psi_{mid}} \tag{6.10}$$

where r_{mid} and ψ_{mid} are the normalizations used for radius and flux. If those normalizations are chosen to coincide with the maxima of both Ω and p, i.e. $\Omega(r_{mid}, z = 0) =$

$\Omega(\psi_{mid}) = \Omega_{max}$ and $p(r_{mid}, z = 0) = p(\psi_{mid}) = p_{max}$, and ψ_0 does not vary much with radius at the midplain, then M_s and M_A correspond to peak values of the sonic and Alfven Mach numbers at midplane. However, if the peak of the Ω and p occur at some radii other than r_{mid} (such as if they have different radial profiles that are maximal at different radii), then M_s and M_A do not correspond directly to the actual peak Mach numbers. In other words, in such a case those values would be computed using the rotation and pressure from two different locations if the maxima do not coincide, and hence M_s and M_A as found in 6.9 and 6.10 would not correspond to the actual Mach numbers at r_{mid}. But even then, M_s and M_A still scale as the actual Mach numbers and can be used to be used to understand how equation (6.8) scales with Mach numbers.

The normalized form of equation (6.8) shows that besides the two Mach numbers, everything else is a geometric profile, only affecting the relative values between two places. In addition to the vacuum field shape and the Mach numbers, only the shapes of the rotation, density, and temperature profiles are required.

6.3 Numerical Solution

The differential operator on the left hand side of equation 6.7 makes this an elliptic partial differential equation that allows for $\tilde{\psi}$ to be solved for with generic PDE solvers. In particular, the PDE Toolbox for MATLAB includes a finite element solver for equations of the form:

$$-\nabla \cdot (C\nabla u) + Au = F \tag{6.11}$$

for the two dimensional u, with non-linear A, C, and F. For cylindrical coordinates, equation (6.7) can be expressed in this form as:

$$A = 0 \tag{6.12}$$

$$C = \frac{1}{r} \tag{6.13}$$

$$F = -\mu_0 r \left[n_0' T + n_0 T' + m_p n_0 r^2 \Omega \left(\Omega \Omega' - \frac{\Omega T'}{2T} \right) \right] \exp\left(\frac{m_p r^2 \Omega^2}{2T} \right) \tag{6.14}$$

This is equation (6.7) expressed in SI units, and not the normalized form in equation (6.8), as no difficulties with numeric stability were observed while allowing easier debugging and manipulation of results without the issue of the Mach number definition used in the normalized form. Hence the inputs are the values of Ω, T and n over the domain.

The PDE equation is solved over a rz plane between the mirror throats and extending out to an r outside the location of magnetic measurements. The solution domain is divided into triangular elements, by dividing a 64x64 rectangular grid across diagonals. The solver allows two boundary conditions: a Dirichlet and generalized Neumann condition. Boundaries on the ends at the mirror throats use the generalized Neumann condition and take the form:

$$\mathbf{n} \cdot \left(\frac{1}{r} \nabla u \right) = 0 \tag{6.15}$$

where $\mathbf{n}$ is a outward normal vector and the $1/r$ factor is inherited from the original PDE. This sets the gradient in the z direction to zero, effectively acting like a symmetric boundary condition at the mirror throats. At the $r = 0$ boundary, the solutions is just fixed to zero. Finally, the $r = r_{max}$ boundary uses a similar Neumann condition as (6.15). As opposed to a Dirichlet boundary, which prevent flux lines from being expelled, this fixes the outward gradient to zero and the outer boundary is moved far enough from the plasma so as not to impact the solution at the location of magnetic measurements.

The right hand side of equation (6.14) is expressed in terms of temperature, rotation, and density profiles over ψ_0. ψ_0 is not explicitly required, only that these profiles and their derivatives are evaluated at a given r and z. The most basic form would be a parabolic profile, which assumes temperature and rotation go to zero at the LGFSs, in terms of $\delta = \psi_{max} - \psi_{min}$ and $\psi_{mid} = \frac{\psi_{max}+\psi_{min}}{2}$:

$$\hat{f} = 1 - \frac{4}{\delta^2}\left(\psi(x,z) - \psi_{mid}\right) \;\; \hat{f}' = -\frac{8}{\delta^2}(\psi_0 - \psi_{mid}) \tag{6.16}$$

This is clamped so that $\hat{f} \geq 0$. Here $\hat{f}$ can represent $\hat{\rho}_0$, $\hat{\Omega}$, or $\hat{T} = \hat{c}_s^2$. Because this is parabolic over $\psi_0 \approx r^2$, the peak of the profile will be skewed toward a larger radius from middle radius between the LGFS. To consider profiles with peaks located at other points from the $\psi_0 = \psi_{mid}$, a skewable profile is also used. Inspired by gamma correction used in computer graphics, this profile has a parameter γ, that is one for zero skew(giving back the above parabolic profile), positive and less than one for skew inward, and greater than one for skew outward. Equal outward and inward skews would be related by $\gamma_{in} = 1/\gamma_{out}$. The resulting profile:

$$\begin{aligned} \hat{\psi} &= \frac{\psi_0(r,z) - \psi_{mid}}{\delta} + \frac{1}{2} \\ \hat{f} &= 1 - 4(\hat{\psi}^\gamma - 1/2)^2 \\ \hat{f}' &= -\frac{8}{\delta}\gamma(\hat{\psi}^\gamma - 1/2)\hat{\psi}^{\gamma-1} \end{aligned} \tag{6.17}$$

Here $\hat{\psi}$ is clamped to the range $0 \leq \hat{\psi} \leq 1$. With $\gamma = 1/\sqrt{2}$, this corresponds roughly to a parabolic profile over r instead of ψ. Examples of radial profiles are plotted in figure 6.1, while an example of the full 2D profile is shown in figure 6.2.

Although equation 6.14 is general enough to allow different profiles for the three functions of flux, they are typically assumed to have the same profile, as is used in the following chapter.

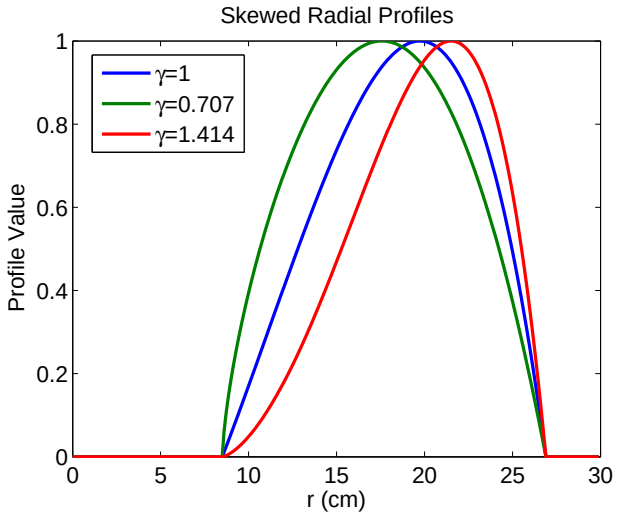

Figure 6.1: Comparison of different γ values used to skew radial profiles, using the ψ_0 for a mirror ratio of 7.8.

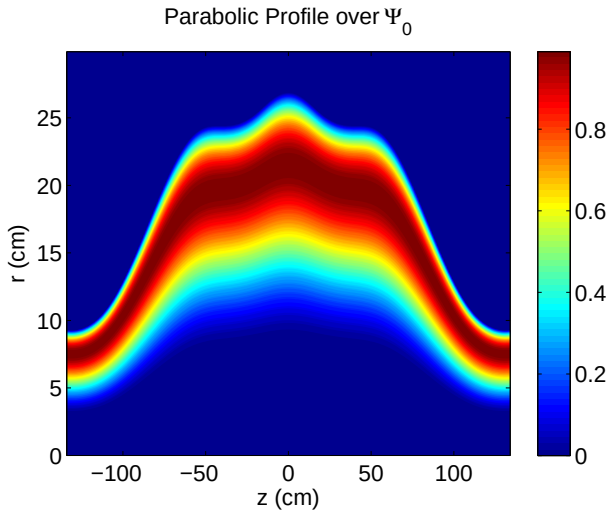

Figure 6.2: Contours of an example of a 2D, parabolic over ψ_0 profile, using the ψ_0 for a mirror ratio of 7.8.

Chapter 7

Results and Discussion

This chapter discusses the application of the MHD solution from the previous chapter to DML measurements, and how the results agree with spectroscopic measurements.

7.1 Fitting

To compensate for difficulties with producing velocity and temperature measurements of the bulk plasma from spectroscopy, the DML data and interferometer data can instead be used to estimate rotation velocity and temperature. This can be done by minimizing square residual of predicted flux measurements using the MHD model discussed in the previous chapter. For a simple case, the temperature and rotation velocities (along with density function $n_0(\psi)$) are assumed to be roughly parabolic over radius (skewed parabola profile from before with $\gamma = 1/\sqrt{2}$. Thus the only remaining free parameters are the peak temperature and rotation velocity.

Fits applied to shots for mirror ratio 7.8 and 3.2 are shown in figure 7.1. For mirror ratio 7.8, this gives a velocity and temperature peak of 115 ± 9 km/s and 13 ± 2 eV, while for mirror ratio 3.2 this gives 152 ± 11 km/s and 20 ± 3 eV. In these cases, fits were applied to DMLs from z positions of 8 cm to 65 cm on a single side of the machine. Although some DMLs have a symmetric pair, since those pairs are in close agreement, adding them to the fitting process would only increase weighting/importance of those DML measurements regardless of them being subject to similar systematic errors as the other DMLs.

Both of the previous results use interferometer measurements at midplane, however

measurements from the second interferometer can also be considered. For higher mirror ratios, the signal to noise ratio is small for the off-midplane interferometer, but for lower mirror ratios this interferometer sees a larger signal. Likewise, spectroscopy measurements are usually done at about the same z as the off-midplane interferometer for low mirror ratios due to less light emitted at midplane compared to high mirror ratio shots. A second such fit done for mirror ratio 3.2 gives a peak rotation velocity of 43 ± 3 km/s and temperature of 1.5 ± 0.3 eV.

The somewhat large difference between the two fits for mirror ratio 3.2, despite the reasonableness of their fit to the DML data, is a result of the MHD model not correctly predicting the density ratio between the two interferometers. In both fits, the result gives a peak sonic Mach number of roughly 3.5, which gives the same shape to each curve. The MHD solution predicts a density ratio between the midplane to off-midplane interferometer of 28 and 5.8 for mirror ratio 7.8 and 3.2 respectively, while the measured ratios were 13 ± 4 and 1.3 ± 0.3. If the model correctly matched the actual density ratio, then constraining the density by a measurement at either axial position would give the same over all density magnitude. However, as the model does not yield the correct density ratio, the overall density magnitude can change by a factor of 3-5 depending which interferometer is used to set the overall density profile magnitude.

7.2 Sensitivity and Errors

The errors in the fit values were determined by refitting data from different shots to see the error from shot-to-shot variation. Additionally, errors in DMLs and density measurements were assumed to be a normal distribution, and fits were repeated with values chosen at random from appropriately scaled normal distributions. The resulting

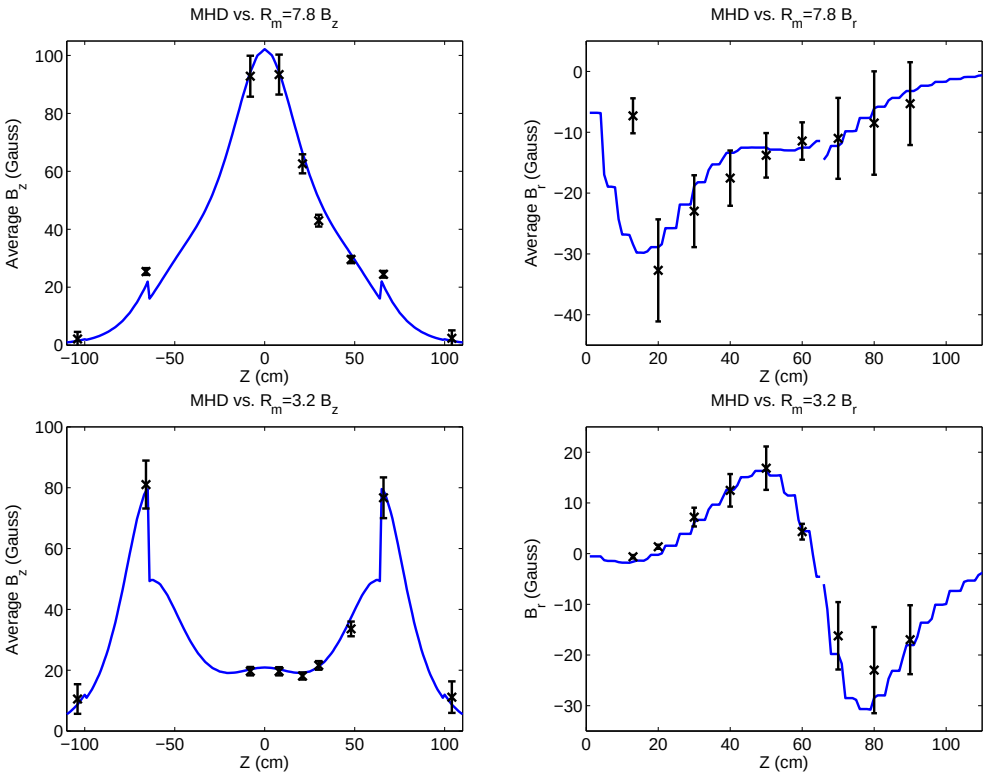

Figure 7.1: These plots show the results of using the solution to the Grad-Shafranov equation to estimate rotation velocity and temperature from DML data. The curves show the resulting magnetic fields given by the solution compared to DML and B_r measurements. The discontinuity at $z = 65$ cm is reflecting the different radial position of loops for $z > 65$ cm due to the reduced vacuum vessel radius there.

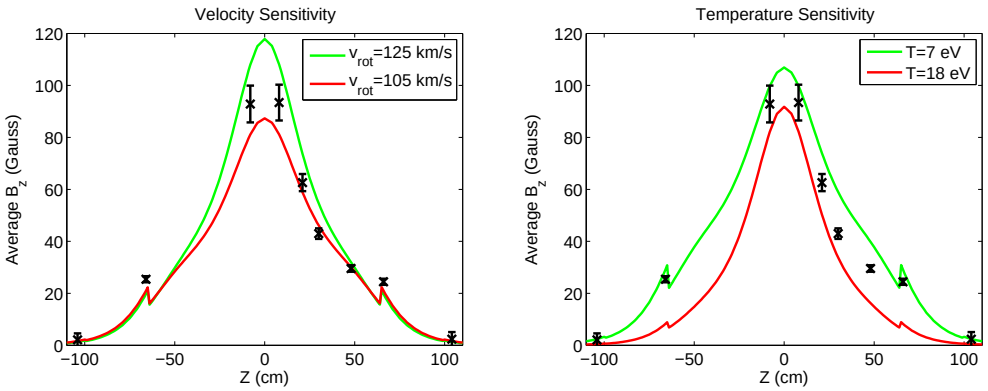

Figure 7.2: These plots show effects of changes in velocity, ±10 km/s, and temperature, ±5 eV, on expected diamagnetism for the example case of mirror ratio 7.8.

errors for velocity and temperature fits were dominated by the effects of error in density measurements.

Plots in figure 7.2 visually show the effects of varying velocity and temperature away from the values fitted for mirror ratio 7.8. This demonstrates how the velocity of the fit is more closely related to the magnitude of the DML measurements (via changing the Alfven Mach number), while the temperature affects the shape and width of the peak. The small changes in velocity result in variations of diamagnetism larger than the DML error bars, hence why the rotation velocity was fitted instead of using the spectroscopy results. The error bars on velocity measurement and the expected differences of uncertain magnitude between impurity velocity and bulk plasma rotation would both be magnified to give a sizable difference from the magnitude of central DMLs.

7.3 Centrifugal Confinement

The effects of centrifugal confinement, one of the primary goals of MCX, can be examined by removing the exponential factor in the Grad-Shafranov equation (equations

6.7 and 6.8). With this factor set to one, the DML data can be refitted, with results plotted in figure 7.3. For both mirror ratios, the fitting algorithm found temperatures of 0.1 eV at the lower boundary of temperature range searched over. Velocities of 210 and 150 km/s were found for mirror ratio 7.8 and 3.2 respectively. These extreme values are a result of attempting to match DML magnitudes and large axial gradients without that exponential factor.

Even ignoring the unrealistic temperature (and high velocity in $R_m = 7.8$ case), the resulting axial profiles are qualitatively different from magnetic data. If considering non-rotating diamagnetism, with $\Delta B_z/B_z \propto \beta$, then $\Delta B_z \propto 1/B_z$. Hence the expelled flux depends mainly on the vacuum field if other parameters are assumed constant along field lines, resulting in axial profiles that reflect the shape of the vacuum field lines. Even with the term due to rotation (second term in 6.8) dominating via the high sonic Mach number, the shape of the axial profile is not variable without the centrifugal confinement factor. So the qualitative differences, such as a center peak broader than that of DML data for the mirror ratio 7.8 B_z profile, can not be eliminated by varying the free parameters. In other words, without that factor, the DML data can not be accounted for, hence the exponential factor in the Grad-Shafranov equation is critical to explaining the axial confinement observed.

7.4 Conclusions

Demonstration of centrifugal confinement has now been shown in multiple ways in MCX. Interferometry continues to show an axial density gradient, with plasma density concentrating at vacuum field minima. Now interferometery has been complemented with DML measurements showing expelled flux around the vacuum minima, and hence a pres-

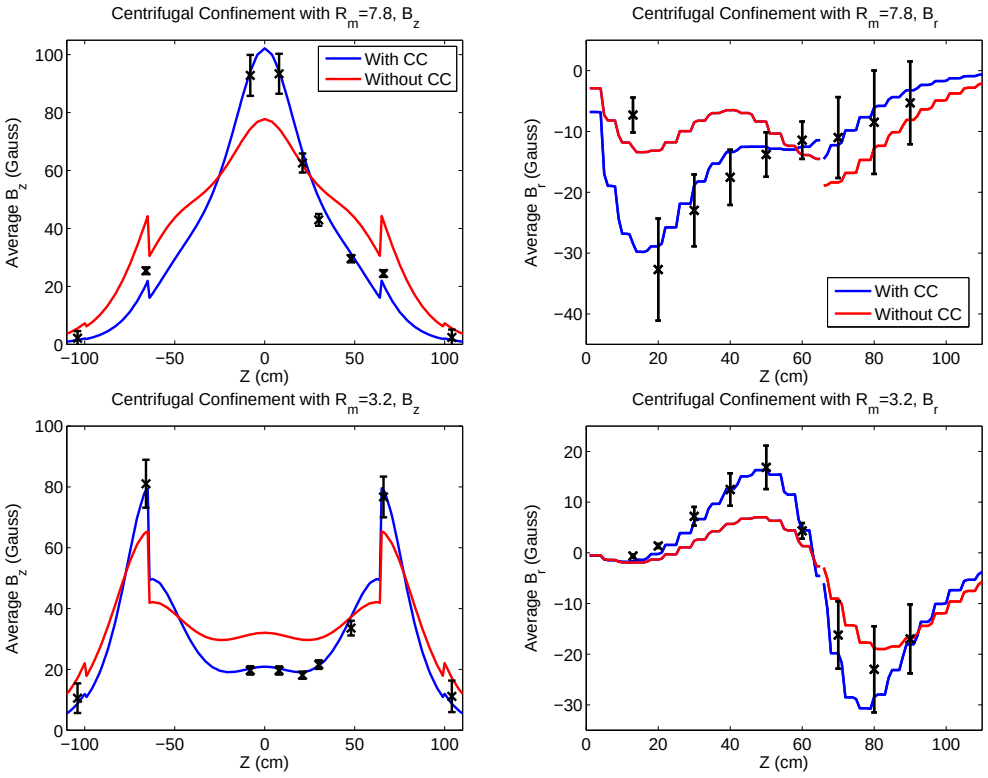

Figure 7.3: In addition to the best fits from MHD shown in blue as previously discussed, in red is shown best fits of the Grad-Shafranov equation without centrifugal confinement (CC).

sure gradient leading to these minima. The axial confinement is observed not only in the typical high mirror ratio cases, but in lower mirror ratios with off-midplane minima. Measurements also support auxiliary goals of velocity shear, and supersonic rotation, with a Sonic Mach number between 1.5 to 2.5, depending on whether temperature is from spectroscopy or from magnetic data.

The application of MHD to the magnetic data also gives a simple reconstruction method, and allows estimation of rotation velocity and temperature. This reconstruction is analogous to reconstruction in tokamaks known as EFIT [27]. Spectroscopic measurements of these can be error prone and sensitive to issues ranging from differences between bulk plasma from impurities to limited visual access to the plasma. Using the magnetic data instead has been shown to provide a simple, reliable estimate of these values.

7.5 Further Work

The central peak in the axial B_z profile is sharper than fitted from MHD, while the density ratio between midplane and off-midplane is measured to be lower than expected. These issues may be the result of the assumption of constant temperature along field lines. Improving matching with the axial profile would likely improve estimates of temperature from DMLs. Measurements suggest higher temperatures, but fitting to DML data gives lower temperatures that keep the axial profile from broadening too much. If an axial temperature profile results in a narrower B_z profile, the temperature estimate from magnetic data would be higher. Adding such axial temperature profiles however would require substantial rewriting of the MHD solver, requiring a custom PDE solver as the resulting equation would no longer be in the convenient elliptical PDE form.

Experimentally, the spectroscopy data could be potentially improved greatly, giving

better estimates of temperature and velocity profiles. One option would be to consider other lines that involve less overlap. And to lower the potential difference between impurities and bulk plasma velocities, helium lines could be considered if a small amount of helium were added to the source gas.

As far as magnetic measurements outside the vacuum vessel, increased accuracy in positioning of loops would be highest priority. This could come from creating better mounting structures for loops, and installing loops in the $10 < z < 50$ cm range with the MS-coils removed. Additional axial density of measurements is unlikely to gain much insight, as the structure of the axial profile already seems well characterized. Additional azimuthal measurements could be useful, even if only to remove the azimuthal perturbations to the field. Finally, all of the loops could be moved inside the vacuum vessel to gain much better frequency response, at the cost of much more complicated construction/mounting and likely larger sources of noise without the low-pass filter nature of the vacuum vessel.

Chapter 8

Azimuthal Magnetic Field

8.1 Background

This chapter discusses an additional magnetic diagnostic: a three-axis internal magnetic probe. The probe differs considerably from the previous DML and magnetic loop, as it is small and located inside the vacuum vessel, allowing the probe to measure a localized field with much higher frequency response, compared to the DMLs' widespread, slow flux measurements.

While designed to make three-axis measurements and have high frequency response, the primary use was to observe millisecond time scale, azimuthal component of the magnetic field: B_ϕ. Previous work has already examined faster timescale, axial component of magnetic field in detail with internal probes [28,29], while millisecond time scale axial and radial field measurements would only incrementally add to external DML and loop measurements. Hence the first priority for the probe was decided to measure the azimuthal component, and to examine on the millisecond scale before examining faster effects.

The primary motivation to measure B_ϕ is to estimate axial currents inside the machine. The metallic core used to generate the electric field to drive rotation is fed current from one end, which returns along the vacuum vessel after traveling across the plasma. By examining B_ϕ at different axial positions, the location or distribution of current return through the plasma can be estimated. As the current return is located on the same end as the current source, ideally there would be no net current through an Ampere loop around the vacuum vessel, hence there would be no external B_ϕ. Although

in practice there are other paths of current return on the MCX vacuum vessel, allowing for some external B_ϕ.

In particular, there is a question of whether the majority of current crosses near the insulators due to plasma-surface interaction there, or if the current crosses near the middle of the machine away from the insulators. The latter question can be further refined into whether the current is leaving symmetrically, or through contact with the plasma limiting jog in the vacuum vessel on only one side.

8.2 Construction

One feature of the probe, is that the measurement for each axis is done by two coils. The two coils in a pair are wound in opposite directions, then connected in series such that magnetic signals add together. In this configuration, any common mode noise due to capacitive coupling of signals into the coils cancels out.

The base of the probe is a 5/16" diameter, 1" length, cylindrical polyethylene bobbin, see figure 8.1. Tracks were cut along the length of a cylinder to hold coils for two of the axes. Fine, 0.004" diameter, magnetic wire is wrapped for 100 loops in each of these four coils along the length of the bobbin (200 loops total for a given axis). The third axis, measuring magnetic field along the length of cylindrical bobbin, consists of 300 turns per coil (600 total) wrapped around the outside of the cylinder along most of the length. The bobbin has a small, threaded hole on one end for attaching onto the end of a longer rod for positioning. A photo of the completed probe is shown in figure 8.2.

The entire assembly is then covered with a single piece of 0.006" thick aluminum foil, followed by shrink wrapping to hold the foil in place. The foil serves as shielding from electrical noise and is grounded at the outer end of the assembly. For positioning

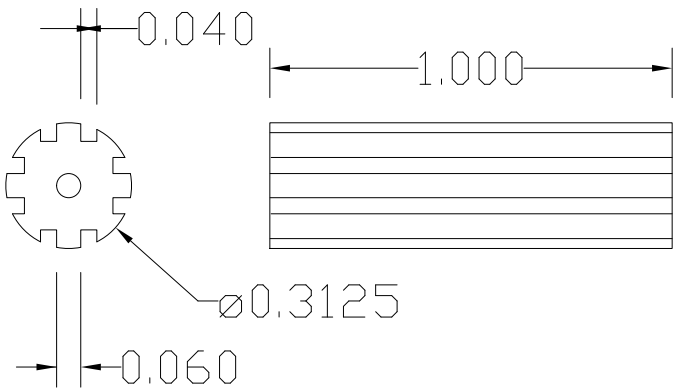

Figure 8.1: A drawing of the bobbin used for the three axes probe.

the probe inside the vacuum vessel, the probe is placed inside a 1/2" quartz tube that has a hemispherical, sealed end. This means the probe remains at atmospheric pressure, but can be placed at radii within the vessel. The quartz tube is attached to the vacuum vessel using a modified Cajon/Ultra-Torr style feedthrough with Viton o-ring seal that allows repositioning along the axis under vacuum. This approach simplifies construction of the probe at the cost of limiting installation positions to locations of vacuum ports.

8.3 Calibration

The calibration of the probe was done with the same Helmholtz coil as was used for magnetometers used to measure the vacuum field in section 2.3.2. However, in this case a frequency response was measured, as shown in figure 8.3. The calibration shown is the factor that converts integrated voltage signal to gauss. Two curves are shown, as there are two axes that can be aligned to B_ϕ.

The calibration factors for these two axes is 3.6±0.3 gauss/Vs and 3.8±0.3 gauss/Vs

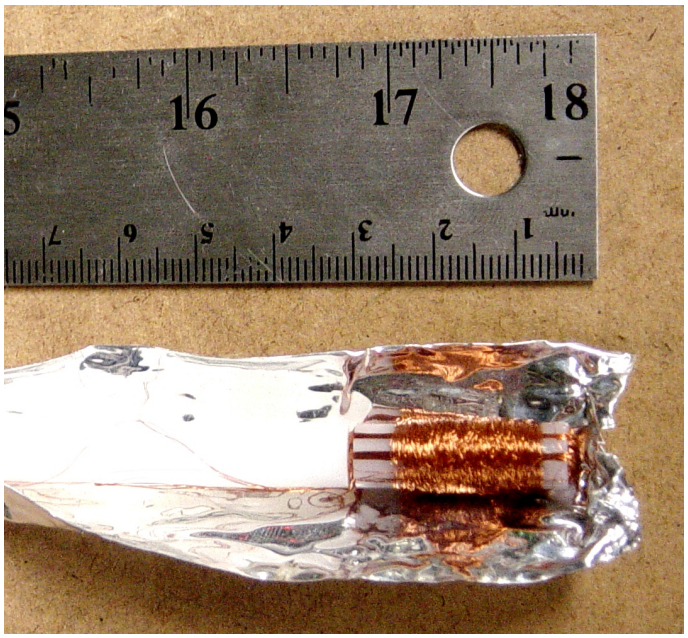

Figure 8.2: This is a photo of the three axes probe. The shielding foil has been partially removed. To the left of the probe is a rod used to position the probe. The coil wrapped around the circular portion of the bobbin would measure B_r, while the coils wrapped lengthwise would measure B_z and B_ϕ. The two visible lengthwise coils both measure the same direction, but have been wound in opposite direction such that they can be combine to subtract out common mode noise.

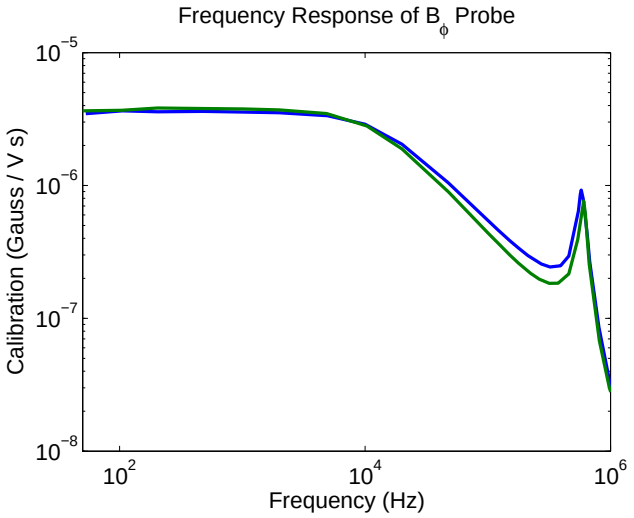

Figure 8.3: This plot shows the frequency response of the two axes on the three axes probe that can be used for B_ϕ measurements.

with a 3 dB cutoff of 14 and 12 kHz respectively. The difference is due to a small difference in area as one set of loops crosses over the top of the other. These cutoffs are sufficient for millisecond timescale measurements. If faster measurements were later required, the shielding foil can be replaced with a thinner foil and the cutoff extended to hundreds of kilohertz.

8.4 Results

The probe was used to measure B_ϕ at three axial locations: at the midplane, and at $z = \pm 80$ cm. As the probe can only be moved to different z locations via a vacuum break, allowing for day-to-day variations, and the radial position is different off-midplane from the midplane position, to compare B_ϕ to the current down the core, the ratio is used:

$$\frac{B_\phi}{B_{core}} = \frac{2\pi r_{probe} B_\phi}{\mu_0 I_{plasma}} \tag{8.1}$$

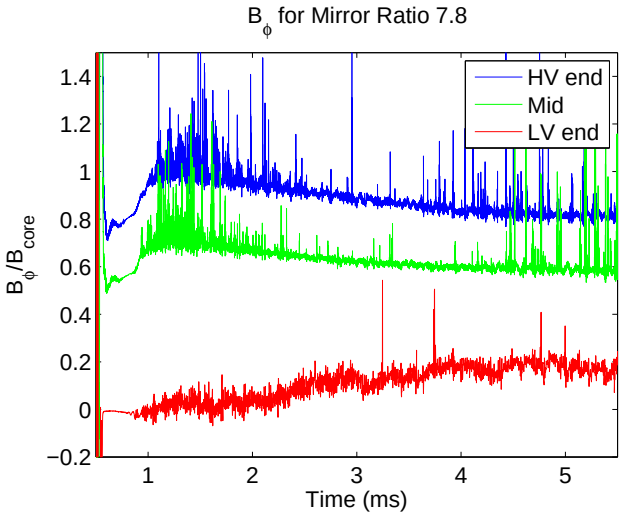

Figure 8.4: These three traces show B_ϕ measured at three different z locations, as compared to the magnetic field that would be created by the full plasma current traveling past the probe.

If this ratio were one, then the B_ϕ is the same as the magnetic field that would be generated by the entire current from the capacitor bank flowing along the core or plasma at the same axial position as the probe. The measurements of this ratio for mirror ratio 7.8 are shown in figure 8.4.

The outermost two measurements show a rough symmetry, with nearly all of the current flowing past the probe position closest to the current input end, and none past the far probe position. This evolves later in the shot until about 20% of the current is flowing to vacuum vessel at each end, leaving about 60% flowing returning via the middle of the vessel (at $|z| < 80$ cm). The middle position shows less symmetry, as a perfectly symmetric distribution of current would result in a value of 0.5 for the middle location. Instead, it looks like more current flows past the midplane than reaches the vessel before reaching the midplane.

Chapter 9

Summary and Conclusions

Several conclusions can be made based on the presented results in this thesis:

- Density measurements agree with previous observations that density is highest at the vacuum field minima, with density peaks up to $4 \times 10^{20} \mathrm{m}^{-3}$ and density ratios between interferometers up to 20.

- Spectroscopy can measure radial profiles of plasma velocity, using an improved deconvolution method treating the profiles as piece-wise linear, giving peak velocities of 105 ± 5 km/s for mirror ratio 7.

- Spectroscopy has also shown an increase in plasma temperature compared to earlier operation, suggesting temperatures as high as 100 eV. This is also evident in the chord-averaged data.

- Measurements of diamagnetism also show concentration of plasma at field minima across different mirror ratios.

- A perturbative solution to an ideal MHD equilibrium was derived and used to reconstruct peak velocity and temperature from density and diamagnetism measurements. The resulting velocity estimates were in agreement with spectroscopic measurements.

- Measurements of the azimuthal magnetic field component show that most of the current fed to the plasma leaves near the middle of plasma, as opposed to flowing across the insulators at the end of the plasma. This suggests that surface breakdown

and cross-field conduction there may not be a major concern for standard MCX operation.

The overall, most important implications come from the results showing plasma is concentrated at field minima and that this is in agreement with ideal MHD. These results demonstrate MCX is achieving its central goal of axially confining plasma in a mirror field geometry. Additionally, further measurement of velocity shear and noting that plasma is stable for durations longer than MHD instability time scales [1], confirm that this goal is being achieved on long time scales, and is not a transient effect.

The use of the MHD solution to derive velocity and temperature from density and magnetic measurements is a particularly practical result for MCX. Spectroscopic measurements of MCX are more involved, as opposed to the magnetic measurements that are typically recorded without further involvement from the operator. Additionally, there are sources of error in the spectroscopic measurement, which can become very limiting in more extreme cases that emit insufficient light or where profiles of interest are not within view of vacuum vessel ports.

However, the present important limitation of the MHD solution is the assumption of constant temperature and rotation along field lines. Exploration of the significance of these assumptions should be a necessary next step, involving the development of a more general solver for the Grad-Shafranov equation. Such work could be complemented by improvement of spectroscopic measurements and especially spectroscopic measurements at multiple axial locations.

The B_ϕ measurements partially addresses a long standing question about the significance of the ceramic insulators at the ends of the plasmas. By showing a large portion of the current does not cross across the insulators, this gives one less way for the insula-

tors to influence the dynamics of the plasma. This may give insight into the benefits of the current insulator design versus older designs if the measurements were repeated with previously used insulators. Measurements of B_ϕ could also be useful to further work on making the machine more symmetric by supplying current through both ends and possibly by use of limiters to address the small asymmetry in current flow near the middle of the machine.

Bibliography

[1] R. F. Ellis, A. Case, R. Elton, J. Ghosh, H. Griem, A. Hassam, R. Lunsford, S. Messer, and C. Teodorescu. Steady supersonically rotating plasmas in the maryland centrifugal experiment. *Physics of Plasmas*, 12(5):055704, 2005.

[2] B. Lehnert. *Nucl. Fusion*, 11(485), 1971.

[3] G. F. Abdrashitov, A. V. Beloborodov, V. I. Volosov, V. V. Kubarev, Y. S. Popov, and Y. N. Yudin. *Nucl. Fusion*, 31(1275), 1991.

[4] A. B. Hassam. Stability of magnetohydrodynamic dean flow as applied to centrifugally confined plasmas. *Physics of Plasmas*, 6(10):3738–3743, 1999.

[5] A. B. Hassam. Velocity shear stabilization of interchange modes in elongated plasma configurations. *Physics of Plasmas*, 6(10):3772–3777, 1999.

[6] C. Teodorescu, W. C. Young, G. W. S. Swan, R. F. Ellis, A. B. Hassam, and C. A. Romero-Talamas. Confinement of plasma along shaped open magnetic fields from the centrifugal force of supersonic plasma rotation. *Phys. Rev. Lett.*, 105(8):085003, Aug 2010.

[7] Yi-Min Huang and A. B. Hassam. Velocity shear stabilization of centrifugally confined plasma. *Phys. Rev. Lett.*, 87(23):235002, Nov 2001.

[8] H. Grad and H. Rubin. Hydromagnetic equilibria and force-free fields. *Proceedings of the 2nd UN Conf. on the Peaceful Uses of Atomic Energy*, 31:190–197, 1958.

[9] J.E. Menard, R.E. Bell, E.D. Fredrickson, D.A. Gates, S.M. Kaye, B.P. LeBlanc, R. Maingi, S.S. Medley, W. Park, S.A. Sabbagh, A. Sontag, D. Stutman, K. Tritz, W. Zhu, and the NSTX Research Team. Internal kink mode dynamics in high- nstx plasmas. *Nuclear Fusion*, 45(7):539, 2005.

[10] L. Guazzotto, J. P. Freidberg, and J. Kesner. Equilibrium beta limits in a dipole configuration. *Physics of Plasmas*, 14(6):062501, 2007.

[11] G. Caudal. A self-consistent model of jupiter's magnetocdisc including effects of centrifgual force and pressure. *J. Geophys. Res.*, 91(A4):4201–4221, 1986.

[12] G. Zimbardo. A self-consistent picture of jupiter's nightside magnetosphere. *J. Geophys. Res.*, 94(A7):8707–8719, 1989.

[13] J. Fukue and R. Okada. Hydrodynamical winds from an accretion disk. *Publ. Astron. Soc. Jpn.*, 42(2):249–267, 1990.

[14] Jonathan Beddoes and J. Gordon Parr. *Introduction to Stainless Steels.* ASM International, Materials Park, OH, 1999.

[15] C. Teodorescu, R. Clary, R. F. Ellis, A. B. Hassam, R. Lunsford, I. Uzun-Kaymak, and W. C. Young. Experimental study on the velocity limits of magnetized rotating plasmas. *Physics of Plasmas*, 15(4):042504, 2008.

[16] Joseph V. Stewart. *Intermediate Electromagnetic Theory*. World Scientific Publishing Co. Pte. Ltd., Singapore, 2001.

[17] John David Jackson. *Classical Electrodynamics*. Wiley, 3rd edition, 1999.

[18] J. Hammon, K. Nielsen, R. Ford, T.H.G.G. Weise, and S. Jungblut. A 30 mj modular 22 kv/44 kv capacitor bank. In *Pulsed Power Conference, 1995. Digest of Technical Papers., Tenth IEEE International*, volume 1, pages 261 –266 vol.1, jul 1995.

[19] Steven G. Roll, editor. *NFPA 70E: Standard for Electrical Safety Requirements for Employee Workplaces*. NFPA, 2000.

[20] Hongfa Ding, Tonghai Ding, Liang Li, Houxiu Xiao, Tao Peng, Xianzhong Duan, and Yuan Pan. Design of a 12 mj capacitor bank of the pulsed high magnetic field facility at hust, wuhan, china. In *Electrical Machines and Systems, 2008. ICEMS 2008. International Conference on*, pages 712 –717, oct. 2008.

[21] Paul M. Bellan. *Fundamentals of Plasma Physics*. Cambridge University Press, 2006.

[22] C W Gowers and C Lamb. A vibration compensated high frequency heterodyne co 2 laser interferometer for plasma diagnostics. *Journal of Physics E: Scientific Instruments*, 15(3):343, 1982.

[23] C. Teodorescu, R. F. Ellis, A. Case, C. Cothran, A. Hassam, R. Lunsford, and S. Messer. Experimental verification of the dielectric constant of a magnetized rotating plasma. *Physics of Plasmas*, 12(6):062106, 2005.

[24] Hans R. Griem. *Principles of Plasma Spectroscopy*. Cambridge University Press, 1997.

[25] B. Blagojević, M. V. Popović, and N. Konjević. Systematic experimental study of the stark broadening of c ii, c iii, n ii, n iii, o ii and o iii spectral lines. *AIP Conference Proceedings*, 467(1):189–190, 1999.

[26] C. A. Romero-Talamás, R. C. Elton, W. C. Young, R. Reid, and R. F. Ellis. Isorotation and differential rotation in a magnetic mirror with imposed e x b rotation. *Physics of Plasmas*, 2012.

[27] Luo Jia-rong. Review of the equilibrium fitting for non-circular tokamak. *Plasma Science and Technology*, 4(2):1183, 2002.

[28] S. Choi, P. N. Guzdar, A. Case, R. Ellis, A. B. Hassam, R. Lunsford, C. Teodorescu, and I. Uzun-Kaymak. Observations and analysis of magnetic fluctuations in the maryland centrifugal experiment. *Physics of Plasmas*, 15(4):042507, 2008.

[29] I. . Uzun-Kaymak, P. N. Guzdar, S. Choi, M. R. Clary, R. F. Ellis, A. B. Hassam, and C. Teodorescu. Nonlinear mode coupling and sheared flow in a rotating plasma. *EPL (Europhysics Letters)*, 85(1):15001, 2009.